


First detection of the atomic ^{18}O isotope in the mesosphere and lower thermosphere of Earth

Helmut Wiesemeyer¹,* Rolf Güsten¹, Rebeca Aladro¹, and Bernd Klein¹
Max-Planck-Institut für Radioastronomie, Auf dem Hügel 69, 53121 Bonn, Germany

Heinz-Wilhelm Hübers²† and Heiko Richter²
German Aerospace Center (DLR), Institute of Optical Sensor Systems, Rutherfordstraße 2, 12489 Berlin, Germany

Urs U. Graf³, Matthias Justen³, Yoko Okada³, and Jürgen Stutzki³
I. Physikalisches Institut, Universität zu Köln, Zùlpicher Straße 77, 50937 Cologne, Germany

 (Received 15 September 2022; accepted 30 November 2022; published 1 February 2023)

In the lower atmosphere of Earth, oxygen contains a higher fraction of the heavy ^{18}O isotope than ocean water does (Dole effect). This isotopic enrichment is a signature of biological activity, set by the equilibrium between oxygenic photosynthesis and respiratory metabolisms in terrestrial and oceanic ecosystems. While the mixing between stratospheric and tropospheric oxygen leads to a slow isotopic homogenization, little is known about the isotopic oxygen enrichment in the mesosphere and thermosphere of Earth. *In situ* measurements from rocket-borne air samplers are limited to altitudes below the mesopause, while higher layers have only been accessible through the analysis of the oxidation of ancient cosmic spherules. Here we report the detection of the far-infrared fine-structure lines ($^3\text{P}_1 \leftarrow ^3\text{P}_2$ and $^3\text{P}_0 \leftarrow ^3\text{P}_1$) of ^{18}O in absorption against the Moon, and determine the $^{16}\text{O}/^{18}\text{O}$ ratio in atomic oxygen from the mesosphere and lower thermosphere in absorption. After correcting for isotopic exchange between atomic and molecular oxygen, our values for the bulk $^{16}\text{O}/^{18}\text{O}$ ratio of 468 and 382 in February and November 2021, respectively, fall significantly below that found in solar wind samples (530 ± 2), and encompass, within uncertainties, the corresponding ratios pertaining to the Dole effect in the troposphere (487), and those found in stratospheric ozone (429 to 466). We show that with existing technology, future, more sensitive measurements will allow us to monitor deviations from isotopic homogeneity in the mesosphere and lower thermosphere of Earth by remote sensing. We demonstrate that the collisional excitation of the fine-structure levels of the ^3P ground-state triplet of ^{18}O may compete with isotopic exchange reactions, implying a deviation from the Boltzmann distribution that would be established under local thermodynamic equilibrium.

DOI: [10.1103/PhysRevResearch.5.013072](https://doi.org/10.1103/PhysRevResearch.5.013072)

I. INTRODUCTION

The ^{18}O isotope of cosmic oxygen emerges as a secondary nucleosynthesis product from helium burning via the triple- α process (the “cosmic carbon factory”), through α capture of ^{14}N and subsequent β^+ decay of the ^{18}F daughter product, while the α capture of ^{12}C yields the main isotope, ^{16}O [1]. Both isotopes of oxygen are mainly produced in high-mass stars, although in their low-metallicity variants the yield of ^{18}O is weak [1,2], while stars of low and intermediate mass destroy ^{18}O in the CNO cycles. The solar $^{16}\text{O}/^{18}\text{O}$ ratio is 511 ± 10 [3], slightly above the terrestrial abundance, 498.7 ± 0.1 , as

defined by the Vienna Standard Mean Ocean Water (VSMOW) [4]. Although the difference is barely significant, solar wind samples confirmed this trend, yielding a solar abundance of $^{16}\text{O}/^{18}\text{O} = 529.7 \pm 1.9$ [5], and validate an earlier finding, 526.8 ± 2.6 , inferred from lunar regolith exposed to the solar wind [6], while rejecting another one, measured in a different sample [7]. It seems the differences emerge from the presence of multiple components in the latter probe. Another contamination may originate from oxygen of poorly known isotopic composition escaping from Earth’s upper atmosphere [8], a scenario corroborated only recently by the discovery of a magnetospheric wind of energetic oxygen ions in its plasma sheet, inferring the exposure of lunar regolith [9].

At lower altitudes, the terrestrial $^{16}\text{O}/^{18}\text{O}$ ratio indeed carries a signature of biological origin, differing significantly from the solar wind value and tracing the planet’s history: While until the early Proterozoic the Precambrian atmosphere contained only trace amounts of O_2 , its concentration increased by several orders of magnitude 2.3 Gyr ago [10]. The origin of this *Great Oxygenation Event* [11] was recently explained by the ecological dynamics involving the competition between anoxygenic photosynthetic bacteria and cyanobacteria, controlled by geophysical evolution [12]. Oxygenic photosynthesis

*hwiese@mpifr-bonn.mpg.de

†Also at Department of Physics, Humboldt-Universität zu Berlin, Newtonstraße 15, 12489 Berlin, Germany.

Published by the American Physical Society under the terms of the [Creative Commons Attribution 4.0 International license](https://creativecommons.org/licenses/by/4.0/). Further distribution of this work must maintain attribution to the author(s) and the published article’s title, journal citation, and DOI. Open access publication funded by the Max Planck Society.

prevailed, driven by the high ability of molecular oxygen (O_2) to accept electrons thanks to its biradical ground-state configuration. The presence of high concentrations of O_2 in planetary atmospheres therefore qualifies as a tracer of biological activity [13,14], provided that the efficient production of O_2 is not hindered by various sinks.

The equilibrium between photosynthesis and respiratory metabolisms and the exchange of O_2 between the land biosphere, the oceans and the atmosphere leads to an enrichment of 23.5‰ of the atmosphere in the ^{18}O isotope with respect to the ocean value (Dole effect [15,16]), while modeled values range from 22.4‰ to 23.3‰ [17]. In the stratosphere, an isotopic exchange occurs between O_2 and CO_2 , correcting the ^{18}O enrichment due to the Dole effect downwards by 0.4‰ [18]. On the other hand, O_3 is isotopically enriched in both ^{17}O and ^{18}O [19–21]. This fractionation is mass independent [22], and ascribed to the competition between the formation of O_3 in the Chapman cycle [23], and a fast exchange reaction, in which the excited O_3 decays back to O_2 and O out of which it formed. If one or both reactants are isotopically heavy, the exchanged oxygen atom is not indistinguishable anymore. Recent quantum-mechanical studies [24–26] achieved a better agreement with experimentally determined reaction rate coefficients [27] than previous calculations [28,29].

For the mesosphere and lower thermosphere (hereafter MLT) of present-day Earth, the distribution of the heavy oxygen isotope is still *terra incognita*; the mesospheric oxidation of cosmic spherules found in Antarctica dates back to up to 2 Myr and was used to determine the enrichment of ^{18}O , yielding a value close to that due to the Dole effect [30]. Our unsatisfactory level of knowledge is partly due to the fact that the MLT is difficult to access, because of its location above the reach of balloon-borne payloads, limited to 53 km altitude [31], and below the operability of very-low-orbit satellites [32]. In particular, we do not know to which level, and to which altitude, transport and mixing processes in the atmosphere entail isotopic homogeneity: While between the ground and up to the lower stratosphere (~ 20 km altitude), bulk $^{18}O/^{16}O$ ratios in O_2 were shown to differ at insignificant levels only [33], values from the lower mesosphere display small yet significant differences from stratospheric and tropospheric ones [34]. For the MLT, such information is still missing, which is also deplorable in view of the evidence of a dynamic coupling between the mesosphere and the thermosphere [35] and of the aforementioned isotopic contamination of near-Earth space. In order to overcome this shortcoming, here we aim at a spectroscopic characterization of the isotopic composition of oxygen in the MLT. Furthermore, from such an investigation one may also expect insight into isotopic exchange reactions between O and O_2 —rightly, because the concentration of O there equals or exceeds that of O_2 , and the concentration of ^{18}O exceeds that of O_3 . Since more than 99.9% of ^{16}O or ^{18}O in the MLT reside in the electronic ground-state 3P , split into triplet substates by spin-orbit interaction of the electrons, such an endeavor calls for remote sensing by far-infrared spectroscopy. The technique was already demonstrated [36–39], but only recently pushed to high enough spectral resolution [40], required to distinguish the fine-structure lines of ^{18}O from those of ^{16}O , separated by a small isotope shift: thanks to the motion of the atomic nucleus around the center of mass, the internal kinetic

energy is split into a normal and, for two or more electrons, a specific mass shift (the latter arises from the mass polarization term). The transition frequencies in the 3P ground-state triplet, 4744.77749 and 2060.06863 GHz for the $J = 1 \rightarrow 2$ and $J = 0 \rightarrow 1$ line, respectively, correspondingly change by 23.88 MHz and 10.61 MHz [41,42].

In the following we report the unambiguous detection of atomic, heavy oxygen, ^{18}O , in the MLT, employing air-borne far-infrared spectroscopy (here and in the rest of the paper, ^{16}O and ^{18}O denote main and heavy oxygen, respectively, in *atomic* form, if not otherwise stated). Thanks to the large population (83.0% and 14.2% in the two lowest levels, 3P_2 and 3P_1 , respectively, relative to the total occupation of the 3P triplet and for thermal equilibrium at a temperature of 180 K, representative for the mesopause [43]), both fine structure lines of ^{16}O appear in strong absorption against a suitably bright and extended background source. The lunar Tranquillitatis basin therefore provides the highest accessible sensitivity for such an experiment.

The experimental setup and the data reduction are presented in Sec. II. The analysis of the spectra and the underlying radiative transfer calculations are detailed in Sec. III, followed by a discussion of our findings in the view of the isotopic composition of the MLT (Sec. IV). The summary Sec. V will provide an outlook to future experiments.

II. EXPERIMENTAL SETUP AND DATA REDUCTION

A. SOFIA/GREAT observations

We used the upGREAT receiver [44] onboard the Stratospheric Observatory for Infrared Astronomy (SOFIA) [45] on flights out of Cologne (Germany) and Palmdale (California). Assisted by the high spectral resolution of upGREAT, we detect the ^{18}O counterparts of both fine structure lines (Fig. 1). The data was acquired during two SOFIA flights. The first data set was obtained 2021 February 24 on SOFIA flight #702, at 12 to 13 km altitude, on a trajectory between the Bay of Biscay and the Azores. The second data set was collected on 2021 November 19 on SOFIA flight #794, over the US state Montana, at 12 km altitude. The GREAT instrument was equipped with the dual color upGREAT low- and high-frequency arrays, LFA and HFA, respectively [44]. The 14 LFA pixels were simultaneously operated in two orthogonal polarizations, sampling seven positions in a hexagonal layout with a median spacing of 32'', and tuned to the rest frequency of the $^3P_0 \leftarrow ^3P_1$ fine structure line of ^{16}O , 2060.06863 GHz [41,42]. For the second flight, only the seven pixels of the vertical polarization could be tuned to the $^3P_0 \leftarrow ^3P_1$ line, while the $^2\Pi_{1/2} J = 3/2 \leftarrow 1/2$ line of ^{16}OH at 1837.816820 GHz was observed (and detected) in the horizontal polarization. The HFA is equipped with seven pixels with a similar layout (median spacing of 13''), and was tuned to the $^3P_1 \leftarrow ^3P_2$ fine structure line of ^{16}O at 4744.77749 GHz [41,42]. The local oscillator (LO) references for heterodyne mixing in the LFA and HFA are provided by solid-state sources (developed by Virginia Diodes Inc.) and quantum-cascade lasers [46] (QCL), respectively. The width of the spectral QCL profile falls below 1 MHz (full width at half-maximum, corresponding to 0.06 km s^{-1}) and is therefore inconsequential for the line profile fitting. In response to thermal fluctuations,

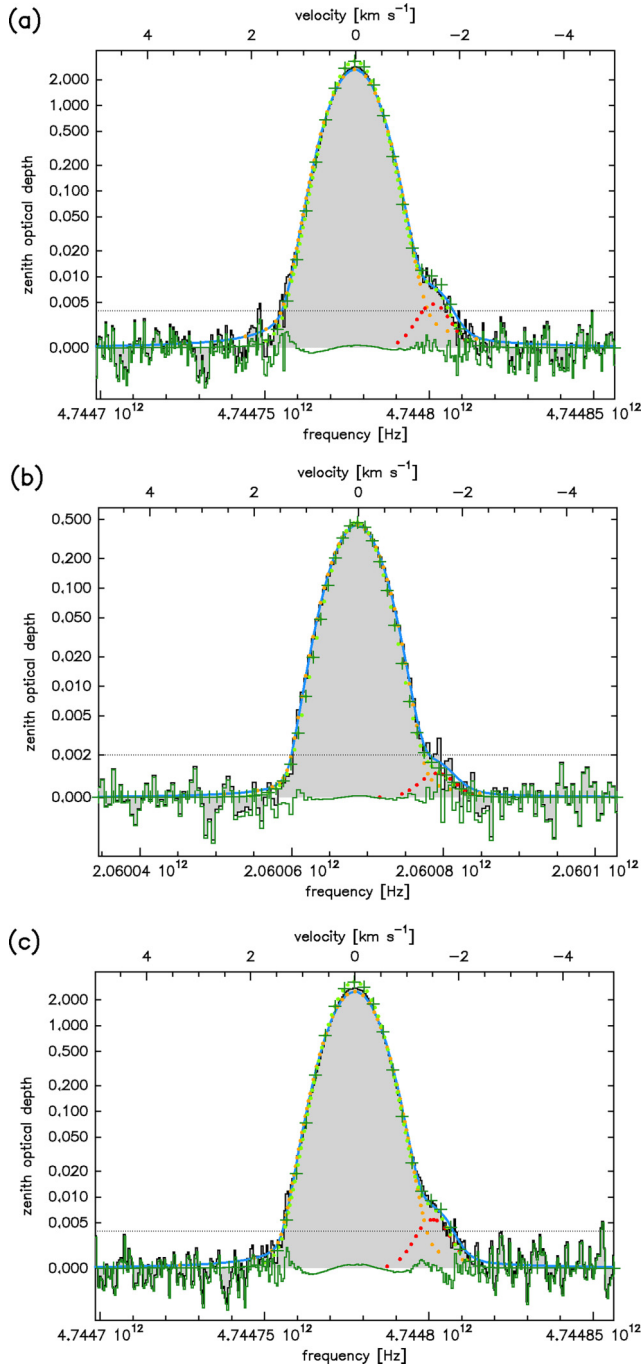


FIG. 1. Optical depth at zenith as observed in the (a) $^3\text{P}_1 \leftarrow ^3\text{P}_2$ and (b) $^3\text{P}_0 \leftarrow ^3\text{P}_1$ absorption line on 2021 February 24 (grey-filled histograms). Note the partially logarithmic ordinates (linear scales below optical depth thresholds, indicated by horizontal-dotted lines, of 0.004 and 0.002 in the $^3\text{P}_1 \leftarrow ^3\text{P}_2$ and $^3\text{P}_0 \leftarrow ^3\text{P}_1$ line, respectively). The line profile fits with a parametrized profile function are overlaid in blue (orange and red dots show the components in ^{16}O and ^{18}O , respectively). The residuals of the fit, as described in Sec. III A and after transformation by Eq. (A10), are shown as green histograms. Lime colored dots display the chemical model for the MSIS 2 model of the MLT after equilibrium is established, including collisional excitation and radiative decay. Green crosses mark the static LTE model for $\delta^{18}\text{O} = 24.15\%$. (c) Optical depth of the $^3\text{P}_1 \leftarrow ^3\text{P}_2$ line on 2021 November 19. Symbols and colors as in (a) and (b).

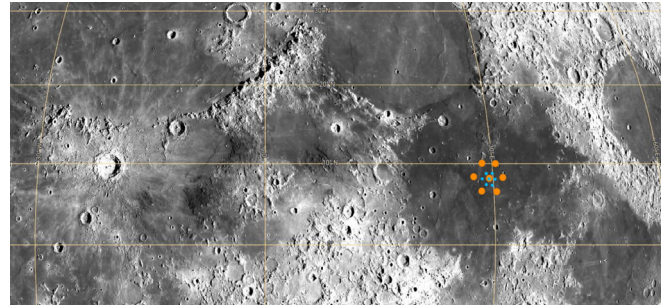


FIG. 2. Zoom into the observed lunar area (top and right are selenographic north and east, respectively), displaying Mare Tranquillitatis to the East, Mare Serenitatis to the North, and crater Copernicus to the West. The overlaid graticule indicates selenographic coordinates. The celestial north pole is at $15:3$ selenographic E from N. The position targeted by our absorption experiment is at 30° E and $8:5$ N. Its distance from the observer at start was 377 677 km (JPL Horizons On-Line Ephemeris System version 4.50). Image from NASA’s Lunar Reconnaissance Orbiter Camera (via quickmap.lroc.asu.edu, credit: NASA/GSFC/ASU). The filled circles in the framed subset show the pixel positions and half- power contours of the low-frequency (orange) and high-frequency arrays (blue)

the QCL was drifting by typically 180 kHz/min, which can be easily tracked by tracing the peak velocity of the mesospheric ^{16}O line in the near field of the array. The total power data was recorded with a granularity of 30 sec. Taking the data at a dump-rate of 10 Hz instead revealed no unresolved LO drift.

Typical single-sideband receiver temperatures in the relevant spectral bandpass interval are 2550 K, 1950 K, and 2840 K in the horizontal and vertical polarizations of the LFA and in the HFA, respectively (February 2021, central pixel medians), and 2150, 2520, and 2940 K in November 2021. The generic resolution of the spectra obtained with the XFFT spectrometers [47] is 244 kHz. For further data analysis they were resampled to a spectral channel separation of 488 kHz.

B. Observing strategy and data assessment

For the targeted position, we selected the center of Mare Tranquillitatis (Fig. 2), at 30° E, $8:5$ N, not too far from the subsolar point at $25:8$ E, $1:5$ S. The area displays large bolometric daytime temperatures [48] in excess of 350 K and a mid-infrared albedo below that of Mare Serenitatis [49]. Thanks to its larger thermal diffusivity, the subsurface regolith of Mare Tranquillitatis reacts faster to changes of the surface temperature than that of Mare Seneritatis [50], leading to a far-infrared brightness peak. The spectra acquired on flight #702 comprise an on-target integration time of 18.5 minutes at 44° to 56° elevation. On flight #794, 17.9 minutes of on-target data was collected, at 51° to 59° elevation. Each on-source integration of 2×15 sec was equally shared with measurements on a reference position $20'$ eastwards. On the February 2021 flight, typical system temperatures (T_{sys} , referred to single-sideband reception at zenith, array medians) were 2730 and 2130 K in the horizontal and vertical polarizations, respectively, of the LFA, and 3200 K in the HFA, with precipitable water vapour columns around $8 \mu\text{m}$. The corresponding quantities pertaining to the November 2021 flight are $T_{\text{sys}} = 2270, 2700,$

TABLE I. Summary of parameters and quantities deduced from line profile fitting. Numbers in parentheses are the numerical values of the combined standard uncertainty $u_c(y)$, referred to the corresponding last digits of the quoted result y . The latter is affected by a random error due to radiometric noise, and by a systematic error arising from a $\pm 2.5\%$ uncertainty (standard deviation) in the ratio of image to signal band gains [63]. For a normal distribution (cf. Fig. 8), the interval $y \pm u_c(y)$ has a 68% confidence level. Results with a weak significance [$<3u_c(y)$] are not reported.

		${}^3P_0 \leftarrow {}^3P_1$	${}^3P_1 \leftarrow {}^3P_2$
ν_0 (${}^{16}\text{O}$) ^a	[GHz]	2060.06863	4744.77749
μ_0 (${}^{18}\text{O}$) ^b	[GHz]	2060.07924	4744.80137
$T_{\text{RJ, Moon}}$ ^b	[K]	330 ± 16	280 ± 28
	2021 February 24		
τ_z (${}^{16}\text{O}$) ^c		0.445(3)	2.61(20)
$10^3 \times \tau_z({}^{18}\text{O})/\tau_z({}^{16}\text{O})$ ^d		2.36(63)	1.82(17)
Γ_L ^e	[MHz]	0.063(8)	0.107(17)
$\Delta\nu_D$ ^f	[MHz]	2.864(15)	6.473(39)
	2021 November 19		
τ_z (${}^{16}\text{O}$) ^c		0.392(5)	2.471(18)
$10^3 \times \tau_z({}^{18}\text{O})/\tau_z({}^{16}\text{O})$ ^d			2.24(23)
Γ_L ^e	[MHz]		0.055(15)
$\Delta\nu_D$ ^f	[MHz]	3.108(21)	6.759(33)

^aRest frequencies from [42].

^bAfter correcting for a coupling efficiency of 0.8. The fluxes correspond to blackbody temperatures of 377 and 383 K at 2060 and 4745 GHz; uncertainties are for conservative 5% and 10% error estimates, respectively.

^cLine-center optical depth at zenith, related to atmospheric transmission \mathcal{T} by $\tau_z = -\ln \mathcal{T}$.

^d ${}^{18}\text{O}/{}^{16}\text{O}$ ratio of line-center optical depths at zenith.

^eLorentz half-width at half maximum.

^fDoppler half-width at half maximum.

and 3140 K in the three subarrays, with typically $9\ \mu\text{m}$ water vapor.

C. Data reduction and calibration

The objective of the data processing is to convert individual spectra (hereafter S_ν), obtained at elevation ϵ , to optical depths at zenith $\tau_{\nu,z}$, assuming a plane-parallel here,

$$\tau_{\nu,z} = -\ln\left(\frac{S_\nu}{S_c}\right) \sin \epsilon, \quad (1)$$

where S_c represents the continuum levels at the frequency of the observed lines, reported in Table I. For a pure absorption spectrum, $\tau_{\nu,z}$ is related to the atmospheric transmission at zenith \mathcal{T} by $\tau_{\nu,z} = -\ln \mathcal{T}$. The dependence of $\tau_{\nu,z}$ on the radiative lifetime of the upper state of the transition under consideration, the line profile, and the lower and upper state populations are given by Eqs. (A3) and (A4). At both frequencies, after correction of the received flux density for losses due to the telescope's central blockage and spillover, characterized by a coupling efficiency of 0.8, the equivalent blackbody temperatures amount to 377 and 383 K at 2060 GHz and 4745 GHz, respectively. While an accurate measurement of the spectral energy distribution of the lunar radiation in the far-infrared is yet missing, we note the satisfactory agreement with the zonal mean bolometric temperature [48] of 389 K.

The fits raw data contain the uncalibrated spectra (binary tables of count rates of 16384 spectral channels per mixer, as processed by the XFFTS [47], and averaged to a sampling specified by the astronomical observation request), accompanied by a descriptive header section. Prior to each

observation of the target, the emission of thermal loads at ambient and cold temperatures (typically 297 and 174 K, respectively) was recorded, and used to convert the count rates to Rayleigh-Jeans equivalent forward-beam brightness temperatures. Prior to further data processing, the frequency scale of the HFA spectra was adjusted, owing to the above-mentioned LO drift. The atmospheric total power, as obtained from the off-target spectra measured within a few seconds after the load scan (to suppress the impact of mixer gain drifts), was compared to the best-fitting emission predicted by the atmospheric model [51] as implemented in the kalibrate task [52] of the *kosma_software* software package. The resulting transmission losses, dominated by stratospheric water vapor, were subsequently used to separate the continuum contributions from the image and signal band, neglecting the slope of the spectral energy distribution of the Moon's far-infrared continuum across the separation of both bands, typically 2.3 to 2.5 GHz in the HFA. In the LFA, depending on mixer performance, sideband separations of 4.0 GHz (for tuning in upper sideband) and 2.6 GHz (tuning in lower sideband, LSB) were used in the horizontal and vertical polarization respectively (in February 2021) and 2.7 GHz (LSB tuning) respectively 2.4 GHz (upper sideband tuning) in November 2021. The signal band spectrum was thereafter corrected for the corresponding transmission loss. Further data reduction was done with the GILDAS software [53] (CLASS package). In the HFA, a polynomial baseline of fifth order was applied to normalize the spectra to the line-to-continuum ratio S_ν/S_c . For the profile of the blended ${}^{16}\text{O}$ and ${}^{18}\text{O}$ fine structure lines, this baseline order is inconsequential, thanks to the small isotope shift and line width, covering only a small ($\sim 5\%$) fraction of the considered frequency interval, and to the absence of

prominent standing wave patterns. In the LFA, however, the emerging baseline pattern should not be removed in the same way, which would result in overshooting corrections, owing to a standing wave between its local oscillators and mixers and to its phase shift between the signal- and image band. We rather characterize the standing wave pattern, with a period of typically 80 MHz, by a linear combination of differential total power spectra, the latter providing a suitable basis for the baseline fit (in order to avoid adding noise to the data, we used wavelet fits to the differential total power spectra). The method was successfully tested and applied to derive a sensitive upper limit to the far- infrared absorption by the heavy hydroxyl radical (^{18}OH) on the sight-line to an astronomical continuum background source [54]. The interpolation of the best-fitting corrections across the blend of the ^{18}O component with that of ^{16}O was found to be uncritical; zero and first order interpolations yield baseline-corrected spectra that are indistinguishable within the noise.

III. RESULTS AND ANALYSIS

Because the isotope shifts and line widths are comparable, the analysis of the spectra, in particular the determination of the $^{16}\text{O}/^{18}\text{O}$ ratio, requires an accurate separation of both components. This can be achieved by two methods, namely, adjusting an empirical line profile to the observed absorption (hereafter referred to as line profile fitting), or modeling the radiative transfer of the lunar continuum radiation through the MLT. While the former method assumes line shapes characterized by a single pressure and temperature, the latter approach allows us to adjust more realistic line profiles and, ultimately, to relax the assumption of a uniform $^{16}\text{O}/^{18}\text{O}$ ratio. In the following, we will apply both methods.

A. Line profile fitting

Driven by the estimate that a ~ 10 -km wide layer centered at the mesopause contributes about 50% of the optical depth with a weakly varying line profile, we first adjust synthetic Voigt profiles to the observed absorption lines, under the assumption of isotopic homogeneity, by minimizing the residuals between the fitted and observed spectra. Although the line profiles are dominated by the thermal (Doppler) broadening due to the Maxwellian velocity distribution at the temperature of the mesopause, it is important to account for the Lorentzian component of the Voigt profile of ^{16}O , owing to its blend with the Gaussian component of the ^{18}O profile (Fig. 3). The ambiguity introduced by this blend can be eliminated thanks to the low-frequency end of the Lorentzian wing of ^{16}O , which is void of a contribution from ^{18}O . The fits are shown in Fig. 1, further details are provided in Appendix A. The results are summarized in Table I, along with explanatory notes. On the 2021 February 19 flight, both fine structure lines of ^{18}O , $^3\text{P}_1 \leftarrow ^3\text{P}_2$ and $^3\text{P}_0 \leftarrow ^3\text{P}_1$, were detected; on 2021 November 19, only the $^3\text{P}_1 \leftarrow ^3\text{P}_2$ transition. All uncertainties are estimated by dedicated Monte Carlo simulations, taking into account both radiometric noise and instrumental parameters required for proper calibration.

At the densities typical of the mesopause, radiative decay and excitation of the ^{16}O atoms are not fast enough to compete

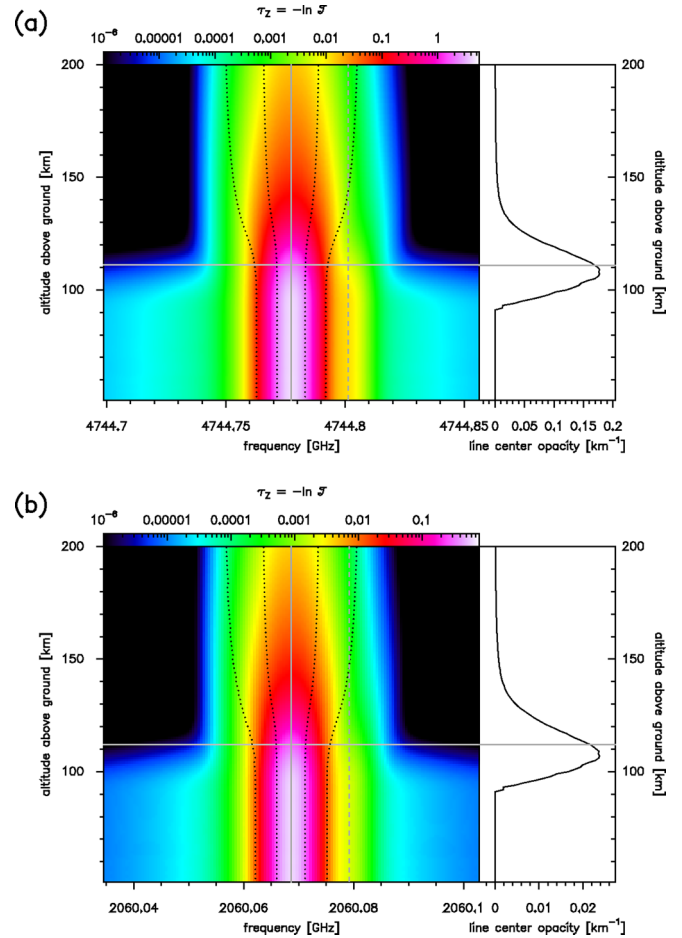


FIG. 3. False-color representation of spectral profiles of the optical depths of the (a) $^3\text{P}_1 \leftarrow ^3\text{P}_2$ and (b) $^3\text{P}_0 \leftarrow ^3\text{P}_1$ lines, as a function of the altitude of a hypothetical observer. The frequencies for the ^{16}O and ^{18}O transitions are indicated by vertical solid and dashed lines respectively. The horizontal-grey lines indicate the altitude where 50% of the final optical depth (as integrated across the spectral profile) is reached, roughly coinciding with the mesopause (around 110 km altitude). The dotted contours are at 50% and 2% of the line-center optical depth at a given altitude; the lower contour indicates a ten times larger optical depth than that expected for ^{18}O . It crosses the frequency of the ^{18}O transition only at 145 km altitude, where the concentration of atomic oxygen drops by an order of magnitude with respect to the mesopause. Below the mesopause, the pressure broadening emerges, yet without destroying the asymmetry of the line profile due to ^{18}O . The inserts to the right show the corresponding altitude profiles of the underlying opacities (i.e., derivative of optical depth with respect to altitude).

with collisions [55]. Under equilibrium between collisional excitation and de-excitation (local thermodynamic equilibrium, hereafter referred to as LTE) and for a Maxwellian velocity distribution of the collision partners, the population of the fine structure levels follows a Boltzmann distribution at the ambient temperature T , such that

$$n_j = g_j \exp\left(\frac{-E_j}{k_B T}\right) \frac{n}{Q(T)} \text{ for } j = 0, 1, 2, \quad (2)$$

where n_j is the density of ^{16}O atoms in the 3P_j state, g_j its statistical weight, E_j its energy above the ground state, and k_B the Boltzmann constant. n is the density of all ^{16}O atoms in the 3P ground state triplet. Higher excited electronic states are negligible here; as discussed in Sec. IV, the fraction of atomic oxygen that resides in the metastable 1D_2 singlet is safely negligible: in the MLT, its abundance falls nine orders of magnitude below that of the 3P triplet [56], with a maximum night-time concentration of 340 cm^{-3} [57]. The distribution given by Eq. (2) is normalized by the partition function $Q(T)$ such that the sum of all n_j yields n . The temperature at which the fit reproduces the observed optical depth ratio of 0.17 between the $^3P_0 \leftarrow ^3P_1$ and $^3P_1 \leftarrow ^3P_2$ lines of ^{16}O amounts to 232 K, which is representative for altitudes of 60 and of 110 km. We note that the prediction of LTE of $^{16}\text{O}(^3P)$ is based on collisions among ^{16}O atoms, ignoring N_2 and O_2 as collision partners, despite their dominance in the MLT. Under this caveat, the underlying study [55] infers that at night-time and low solar and geomagnetic activity, LTE is believed to hold up to 350 km altitude, and to more than 600 km at high activity. The fitted Doppler widths agree, within errors, between both 3P transitions. The optical depth ratios of the $^3P_1 \leftarrow ^3P_2$ lines of ^{16}O and ^{18}O infer abundance ratios of $^{16}\text{O}/^{18}\text{O} = 583 \pm 54$ and 474 ± 49 for 2021 February 19 and November 21, respectively (numerical values after the \pm symbol refer to combined standard uncertainties). The corresponding ratio obtained from the $^3P_0 \leftarrow ^3P_1$ line on the former flight amounts to 449 ± 120 . The measurement uncertainties are typical of isotope ratios deduced from remote-sensing experiments applying submillimeter- or infrared spectroscopy, e.g., towards the atmospheres of planets, moons or comets in the solar system [58–60], while higher accuracies are usually achieved with isotope ratio mass spectroscopy (e.g., [61] for the Martian atmosphere) unless conducted under special conditions (e.g., on comet 67P [62]). Figure 4 displays a synopsis of the experimental determinations of $^{16}\text{O}/^{18}\text{O}$ quoted in this paragraph. With the data presently at hand, we cannot decide whether the difference between the $^{16}\text{O}/^{18}\text{O}$ ratios obtained from the $^3P_1 \leftarrow ^3P_2$ lines reflects our measurement uncertainty or rather seasonal variations, which would be conceivable given that the underlying data, separated in space and in time, refer to chemically different conditions.

B. Radiative transfer

As an alternative to the above line profile fitting, in the following we adjust spectra synthesized by means of radiative transfer along the sightline crossing the MLT. This allows us to more accurately describe the line formation along the sightline, demonstrated in Fig. 3, but requires a model for the profiles of temperature, pressure and ^{16}O concentration. The former two quantities are taken from the MSIS 2 model [43], as traced by the actual sightlines observed on 2021 February 24 and November 19 (Fig. 5). We will adopt an educated guess for the $^{16}\text{O}/^{18}\text{O}$ ratio in the MLT, and then verify whether the modeled absorption spectra agree with the observed ones at a satisfactory level. In order to facilitate the comparison with literature, we use the conventional $\delta^{18}\text{O}$ notation to measure the fractional abundance of ^{18}O , defined by $\delta^{18}\text{O} = (X(^{18}\text{O})/X(^{18}\text{O})_{\text{VSMOW}} - 1) \times$

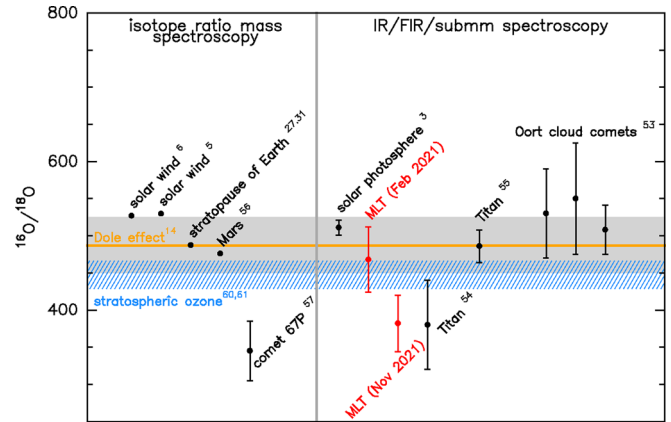


FIG. 4. Synoptic presentation of $^{16}\text{O}/^{18}\text{O}$ ratios in the solar system, separated into isotope ratio mass spectroscopy (left) and (far-)infrared and submillimeter spectroscopy (right), with appropriate labels enhanced by a selection of colors. The study at hand is shown in red and refers to the $^3P_1 \leftarrow ^3P_2$ transition on 2021 February 24 (left) and 2021 November 19 (right), after corrections for non-LTE and isotopic exchange with O_2 . The orange bar indicates the isotope ratio due to the Dole effect. The gray-shaded area indicates the range of $\delta^{18}\text{O}$ values in the troposphere and stratosphere of Earth, lunar, and meteoritic samples; the blue-hatched portion refers to $\delta^{18}\text{O}$ values from stratospheric ozone [67,68]. Error bars refer to $\pm 1\sigma$ and are shown if they exceed the symbol size. Label superscripts indicate the used reference.

1000‰, where $X(^{18}\text{O})$ is the $^{18}\text{O}/^{16}\text{O}$ ratio in the MLT, and $X(^{18}\text{O})_{\text{VSMOW}} = 2005.2 \times 10^{-6}$ that of the VSMOW standard [4]. We use $\delta^{18}\text{O} = 24.15\text{‰}$, obtained from a laboratory analysis of cosmic spherules found in Antarctica [30]. Although their oxidation in the mesosphere dates back to up to 2 Myr ago and may not necessarily be relevant for the study at hand, values around $\delta^{18}\text{O} = 23\text{‰}$ were also obtained by *in situ* measurements of O_2 at 60 km altitude [34]. As we will see, within reasonable limits the exact choice is inconsequential for the analysis. Furthermore, these $\delta^{18}\text{O}$ values are within the uncertainties of the estimate deduced from the direct line profile fitting of our data.

The model reproduces the optical depth spectra shown in Fig. 1, after scaling down the atomic oxygen densities for 2021 February 24 and November 19, by factors 0.75 and 0.65, respectively. Similar dissimilarities between the empirical and experimental methods have been reported [64,65], and are also apparent (Fig. 5) in comparison with broadband-emission radiometry [66]. The Doppler component of the Voigt profile is given by the thermal linewidth resulting from the temperature profile of the MSIS 2 model, while for the Lorentzian component we adopt the pressure broadening coefficient obtained from the line profile fitting (Table I, details are given in Appendix A). The fairly good agreement between the modelled and observed optical depth spectra suggests that LTE holds for both isotopes, at least throughout the altitudes dominating the line formation and within the noise level in the underlying data. As we discuss now, for ^{18}O , the conjecture of LTE should not be taken as a proof, though.

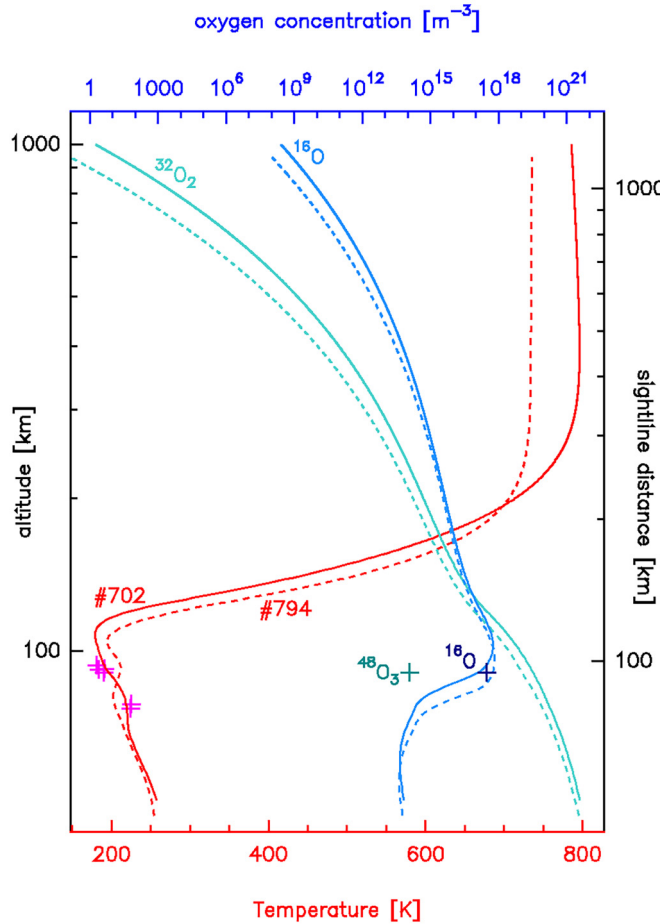


FIG. 5. MSIS 2 model [43] for SOFIA flights #702 and #794 on 2021 February 24 (solid lines) and November 19 (dashed lines), respectively. The displayed profiles can be distinguished either by color or line style and labels. Temperature (lower abscissa) and concentrations of atomic and molecular oxygen (upper abscissa) are shown against altitude above ground (left ordinate) or corresponding to a given position on the sightline (right ordinate). The base point of the sightlines and their elevations correspond to leg medians (geographic longitude 21° W, latitude 43° N, elevation 49° for 2021 February 24, and longitude 110° W, latitude 46° N, elevation 55° for 2021 November 19). For flight #794, data obtained close in space and time by broadband emission radiometry (SABER instrument aboard the TIMED satellite) are marked as crosses (temperature in magenta, and the concentrations of ^{16}O and ozone in dark blue and cyan, respectively). Their analysis is described in [66].

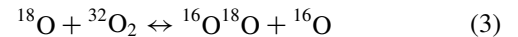
IV. DISCUSSION

The optical depth ratios $X_{0\leftarrow 1}$ and $X_{1\leftarrow 2}$ for the 2021 February 24 flight, $2.36(63) \times 10^{-3}$ and $1.82(17) \times 10^{-3}$, respectively, are not easily conceivable, because under LTE an equality is expected. Unless isotope-selective effects in the actual line formation are at work, this result would infer a non-LTE level occupancy in the $^3\text{P}_j$ levels of ^{18}O . The probability that the isotope ratio pertaining to the $^3\text{P}_0 \leftarrow ^3\text{P}_1$ transition exceeds the best-fit ratio for the $^3\text{P}_1 \leftarrow ^3\text{P}_2$ transition amounts to 80.4%. The probability that this holds for any pair of values is 79.6% (the underlying estimators are discussed in Appendix D). While these probabilities are still too low to

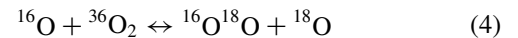
rigorously conclude whether $^{18}\text{O}(^3\text{P})$ is in LTE or not, it is clear that the direct spectroscopic determination of a $^{16}\text{O}/^{18}\text{O}$ ratio using the ^3P fine structure lines is only possible if the excitation of both isotopes is in LTE. Otherwise, a correction is required that accounts for the deviations in the level populations entailed by non-LTE. A discussion of the rates setting the collisional excitation will therefore be instructive and is provided in Appendix B. In summary, at the mesopause the lifetime against collisional de-excitation of the $^3\text{P}_1$ level of atomic oxygen amounts to 1.6 msec, and to 40 msec for the $^3\text{P}_0$ level, falling below the spontaneous emission rate by seven orders of magnitude. Any process perturbing the resulting LTE level populations must therefore compete with these timescales. As we demonstrate in the following, the speed of isotopic exchange and ion-neutral reactions involving atomic and molecular oxygen is of particular interest here. The atomic fraction of oxygen in the MLT corresponding to the altitude profiles shown in Fig. 5 is given in Table III.

A. Isotopic exchange reactions

In the atmosphere [69,70] and some interstellar environments [54], fast exchange reactions indeed contribute substantially to isotopic substitutions. Under the conditions in the MLT, they compete with collisional excitation, as we demonstrate in the following (for brevity, ^{16}O refers to the ^3P ground state triplet of atomic oxygen, ^{18}O to its isotopically heavy equivalent, $^{32}\text{O}_2$ to $^{16}\text{O}^{16}\text{O}$, and $^{36}\text{O}_2$ to $^{18}\text{O}^{18}\text{O}$). The reactions



and



are particularly fast [27,71], and can therefore be approximately decoupled from the other reactions of the odd oxygen network, including its photochemistry. At 95 km altitude, where the ^{16}O concentration in the MSIS 2 model for 2021 February 24 is largest, the lifetime of ^{18}O against replacement with ^{16}O via reaction (3) amounts to 31 msec, falling below the lifetime against collisional de-excitation of $^{18}\text{O}(^3\text{P}_0)$ by 25%. In contrast, the lifetime of O in reaction (4) is 27 hours, assuming a stochastic (i.e., unfractonated) $^{36}\text{O}_2$ concentration $[^{36}\text{O}_2] = [^{18}\text{O}]^2 = 4.2 \times 10^{-6}$. This implies that there are too few reaction partners to allow reaction (4) to modify the LTE population of ^{16}O , while $^{18}\text{O}(^3\text{P}_0)$ has an equal chance to be replaced by ^{16}O via (3) or to undergo a collision, entailing a non-LTE population of ^{18}O . Such an estimate is necessarily crude, not least because neither reaction is resolved for the ^3P fine structure.

Notwithstanding, with the data at hand we can approximate a correction of the $^{16}\text{O}/^{18}\text{O}$ ratio from Sec. III, valid only for atomic oxygen, it does not reflect the isotopic enrichment in molecular oxygen. For such a correction, we may neglect reaction (4): Because, unlike reaction (3), it involves two heavy oxygen nuclei, it will be ~ 500 times slower than Eq. (3). Under chemical equilibrium (this assumption will be substantiated below, along with the neglect of ozone and carbon dioxide), the $^{16}\text{O}/^{18}\text{O}$ ratio R in the oxygen reservoir of the MLT can be

TABLE II. Fine-structure state resolved column densities, $\delta^{18}\text{O}$ values with respect to the VSMOW standard [4] and coefficients for departure of ^{18}O from LTE, as resulting from the chemical model, including reactions (3) and (4), collisional excitation and radiative decay, for 2021 February 24.

	$^3\text{P}_2$	$^3\text{P}_1$	$^3\text{P}_0$
	LTE and $\delta^{18}\text{O} = 24.15\%_o^a$		
$N(^{16}\text{O}) [10^{17} \text{cm}^{-2}]$	7.4	1.5	0.3
$N(^{18}\text{O}) [10^{14} \text{cm}^{-2}]$	15.1	3.0	0.6
	Chemical model (at $t = 16.7 \text{ d}^b$)		
$N(^{18}\text{O}) [10^{14} \text{cm}^{-2}]$	13.0	3.0	0.7
$N(^{16}\text{O}^{18}\text{O}) [10^{18} \text{cm}^{-2}]$	8.6.....
$\delta n(^{18}\text{O}, ^3\text{P}) [\%_o]^c$	-140	33	177
$\delta N(^{18}\text{O}, ^3\text{P}) [\%_o]^c$	-118	17	120
$N/N_{\text{LTE}}(^{18}\text{O})^e$	0.86	0.99	1.09
$\delta N(^{16}\text{O}^{18}\text{O}) [\%_o]^f$	22.....

^aFor MSIS 2 sightline profile of $^{16}\text{O}(^3\text{P})$ concentration and temperature.

^bTime after which chemical model reaches equilibrium at all altitudes. The underlying isotopic bulk composition is $\delta^{18}\text{O} = 24.15\%_o$ [30]. For details see Appendix C.

^cSubstate-resolved volume-density specific $\delta^{18}\text{O}$ at mesopause (defined by the temperature minimum, 179 K, as given by MSIS 2 model).

^dAs (c) but referring to column density.

^eDeparture of substate-resolved column densities from their values expected under LTE.

^f $\delta^{18}\text{O}$ of $^{16}\text{O}^{18}\text{O}$ vs $^{32}\text{O}_2$ column density (referred to the number of nuclei). Corresponds to volume-specific value at 61 km altitude, cf. [34].

deduced from that in atomic oxygen, $X = [^{16}\text{O}]/[^{18}\text{O}]$, via

$$[^{18}\text{O}] \cdot [^{32}\text{O}_2] \cdot k_{1a}(T) = [^{16}\text{O}] \cdot [^{16}\text{O}^{18}\text{O}] \cdot k_{1b}(T) \quad (5)$$

and, by definition,

$$[^{16}\text{O}^{18}\text{O}] + [^{18}\text{O}] = (2[^{32}\text{O}_2] + [^{16}\text{O}])/R, \quad (6)$$

where k_{1a} and k_{1b} denote the reaction rate coefficients for the forward and backward direction, respectively, of reaction (3) at temperature T , and squared brackets the concentrations of reactants and products. Combining Eqs. (5) and (6) yields

$$R = X \cdot \frac{2[^{32}\text{O}_2] + [^{16}\text{O}]}{[^{32}\text{O}_2] \cdot \frac{k_{1a}}{k_{1b}} + [^{16}\text{O}]} \quad (7)$$

It is important to note that the correction factor [the fraction on the right-hand side of Eq. (7)] does not depend on the isotope ratio, and can therefore be calculated from the MSIS 2 model providing the concentrations of $^{32}\text{O}_2$ and ^{16}O and the temperature profile. After integration along the sightline, it amounts to 0.8918 and 0.9037 for the conditions pertaining to the 2021 February 24 and November 19 measurements, respectively.

For a better understanding of a departure of $^{18}\text{O}(^3\text{P}_j)$ from LTE, we formulate a linear network consisting of reactions (3) and (4) and of the rate equations for the collisional occupation of the $^{18}\text{O}(^3\text{P}_j)$ levels [correcting the $^{16}\text{O}(^3\text{P}_j)$ collisional rate coefficients estimated above for the small isotopic mass shift]. Because at the mesopause the concentration of ozone falls below that of ^{16}O by four orders of magnitude [56,66] (cf. Fig. 5) and more at higher altitudes, and by two orders of magnitude below those of ^{18}O and $^{16}\text{O}^{18}\text{O}$, reactions where a third body is used to stabilize the ozone complex forming in the above reactions (Chapman cycle [23]) are neglected. Likewise, we omit isotopic exchange reactions [72] with mesospheric CO_2 ; whether its concentration [73] is large enough for them to be important remains to be demonstrated. With respect to their concentration in the MLT, the uptake of ^{16}O and $^{32}\text{O}_2$ by the chemistry involving ^{18}O , $^{16}\text{O}^{18}\text{O}$, and $^{36}\text{O}_2$ is quantitatively small, and controlled by the total number of ^{18}O nuclei, fixed with respect to that of ^{16}O [Eq. (6)]. For consistency with the radiative transfer model from Sec. III, we adopt $\delta^{18}\text{O} = 24.15\%_o$. We also include collisions between ^{16}O and ^{18}O , again adjusting published collisional rate coefficients

TABLE III. $\text{O}(^3\text{P})$ fraction in the MLT.

Altitude ^a [km]	Atomic fraction [%] ^b	
	2021 February 24	2021 November 19
85	0.5	0.8
90	3.3	4.5
95	9.4	11.3
100	17.6	19.7
105	26.6	29.0
110	36.6	39.5
115	45.8	49.7
120	53.5	58.5
130	65.1	71.1
140	73.2	79.2
150	79.2	84.6
160	83.6	88.4
170	87.0	91.2
180	89.7	93.2
190	91.7	94.7
200	93.4	95.9
220	95.7	97.5
240	97.2	98.4
260	98.2	99.0
280	98.8	99.4
300	99.2	99.6

^aLayers above 300 km contribute 0.1% to the column density of $\text{O}(^3\text{P})$.

^bDefined as $[\text{O}(^3\text{P})]/([\text{O}(^3\text{P})] + [\text{O}_2]) \times 100\%$. Concentrations (in square brackets) are from MSIS 2 [43].

[55] to account for the isotopic mass shift. Further details on the chemical model, including the numerical procedure and its underlying reaction and collision rates, can be found in Appendix C. The underlying pressure and temperature profiles, as well as the concentrations of ^{16}O and $^{32}\text{O}_2$, are given by the MSIS 2 model for the corresponding flight date and aircraft position. With the obtained $\delta^{18}\text{O}$ profile, we then calculate the radiative transfer so as to allow for a comparison with the observed spectra.

The resulting optical depth spectra (Fig. 1) of the $^3\text{P}_1 \leftarrow ^3\text{P}_2$ and $^3\text{P}_0 \leftarrow ^3\text{P}_1$ lines describe the observations as closely as those obtained from LTE in the $^{18}\text{O}(^3\text{P})$ triplet. For 2021 February 19, the optical depths predicted by the chemical model at the peaks of the ^{18}O components differ from the observed ones by -9.5% and -1.7% in $^3\text{P}_0 \leftarrow ^3\text{P}_1$ and $^3\text{P}_1 \leftarrow ^3\text{P}_2$ respectively, while under LTE the corresponding numbers amount to $+1.4\%$ and $+17\%$. Given the higher significance of the ^{18}O detection in the $^3\text{P}_1 \leftarrow ^3\text{P}_2$ transition, this suggests that non-LTE provides a better description of the observed ^{18}O profiles than LTE does. Only an increased sensitivity will facilitate a more stringent conclusion. As expected, populating the $^{18}\text{O}(^3\text{P}_j)$ levels only through their state-selective production via the back- reaction of (3) and the forward direction of (4), neglecting collisional excitation and radiative decay, fails to reproduce the optical depths observed in either transition.

The resulting state-resolved column densities for LTE and non-LTE are summarized in Table II. The correction to obtain the bulk $^{16}\text{O}/^{18}\text{O}$ ratio in the total oxygen reservoir of the MLT from that in the atomic species amounts to 0.8901, in for practical purposes sufficient agreement with the result from Eq. (7). This number refers to chemical equilibrium; however, as shown in Fig. 6, the correction converges rapidly, to a relative change below 0.02% after 77 sec on 2022 February 24 and 54 sec on 2022 November 19. This is sufficiently fast to quickly respond to varying conditions; the criterion for convergence has been chosen to compare with the precision of the $\delta^{18}\text{O}$ value of the VSMOW standard. This result is fairly robust against deviations from the assumed bulk $^{16}\text{O}/^{18}\text{O}$ ratio; introducing offsets of $\pm 2\%$ to the assumed $\delta^{18}\text{O} = 24.15\%$ changes these timescales by merely 0.1 sec. Under non-LTE and at the mesopause, the $^3\text{P}_2$ ground state of ^{18}O is under-populated with respect to its LTE equivalent, while the $^3\text{P}_0$ level is over-populated. The $^3\text{P}_1$ level remains close to its LTE population. This statement also holds for the state-resolved column densities, integrated along the sightline. At 61 km above ground, the modelled ^{18}O abundance in the diatomic reservoir formed by $^{16}\text{O}^{18}\text{O}$ amounts to $\delta^{18}\text{O} = 22.0\%$, which agrees reasonably well with the 23.4% obtained from *in situ* mass spectroscopy [34] at that altitude, although the isotopic exchange with O_3 , becoming increasingly important with decreasing altitude, is neglected. Depending on the altitude and the $^3\text{P}_j$ level, in $^{18}\text{O}(^3\text{P})$ our simple model reaches a dynamical equilibrium after 1.5 to 14 days. This is less than the lifetime of atomic and molecular oxygen in the mesopause and above, justifying the assumption of chemical equilibrium [Eq. (5)]. However, the lifetime against transport by zonal winds and vertical diffuse mixing is shorter [74], especially in the isotopic substitutions of O_2 , reaching equilibrium only after $^{18}\text{O}(^3\text{P})$ does. Therefore, although our

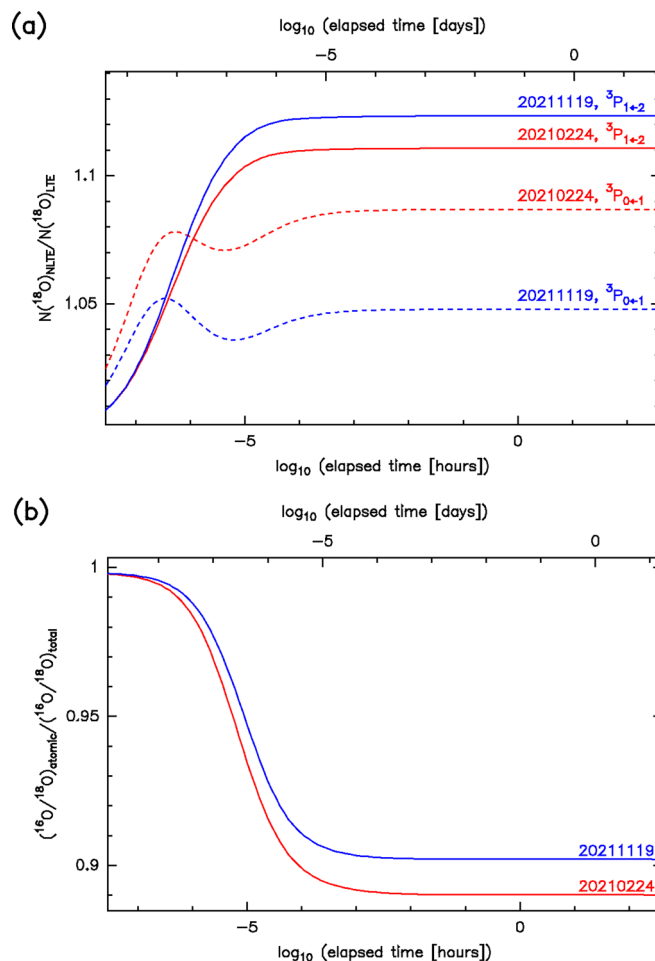


FIG. 6. Time evolution of correction factors for (a) non-LTE in the fine-structure levels of ^{18}O , (b) partitioning of the ^{18}O enrichment into atomic and molecular oxygen.

demonstration of the fine structure state-selective competition between collisions and isotopic exchange reactions reproduces the observed optical depth spectra, it should not be taken too far. In particular, future models are to be embedded in a wider range of environmental conditions.

For the study at hand, we need to address the error introduced in the $^{16}\text{O}/^{18}\text{O}$ ratio deduced from line profile fitting by assuming LTE. With the chemical model and the underlying MSIS 2 models at hand, one obtains for the $^3\text{P}_1 \leftarrow ^3\text{P}_2$ line correction factors of 1.11 and 1.12 for 2021 February and November, respectively. For the $^3\text{P}_0 \leftarrow ^3\text{P}_1$ line, the corresponding figures amount to 1.09 and 1.05. These numbers refer to chemical equilibrium, but, like the correction to isotopic bulk fractionation, converge fast, after typically 5 sec in the $^3\text{P}_1 \leftarrow ^3\text{P}_2$ transition, and 25 sec in the $^3\text{P}_0 \leftarrow ^3\text{P}_1$ transition (Fig. 6, again applying a 0.02% convergence criterion). Varying the $\delta^{18}\text{O}$ bulk value of 24.15% by offsets of $\pm 2\%$ changes these timespans by 0.1 and 0.5 sec, respectively, which does not impact the discussion at hand. The fact that the correction in the former, stronger line varies only weakly between the two observing campaigns, tracing different sightlines in different seasons, lends hope that even out of LTE the $^3\text{P}_1 \leftarrow ^3\text{P}_2$ absorption spectrum, upon deeper integrations at higher altitude, will be capable of providing

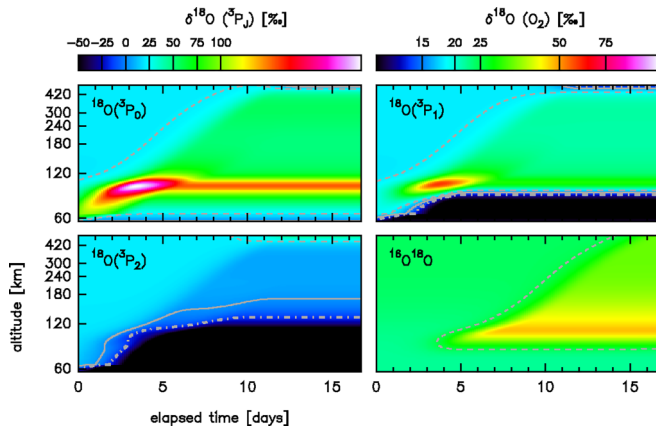


FIG. 7. Color-scale representation of chemical evolution of ^{18}O enrichment in the $^3\text{P}_0$, $^3\text{P}_1$, and $^3\text{P}_2$ levels (top and bottom left), and in $^{16}\text{O}^{18}\text{O}$ (bottom right), with respect to their respective parent species. Shown are $\delta^{18}\text{O}$ values relative to the VSMOW standard [4], against time (abscissae) and altitude (ordinates), for the reservoir formed by ^{16}O and fine-structure resolved ^{18}O , and for that containing $^{16}\text{O}^{18}\text{O}$ and $^{32}\text{O}_2$ (bottom right, referred to number of nuclei). The grey dot-dashed, solid, and dashed contours indicate $\delta^{18}\text{O} = -25.0, 0.0$ and $+25.0\%$. Underlying concentrations of $\text{O}(^3\text{P})$, O_2 ($X^3\Sigma_g^-$) and N_2 ($X^1\Sigma_g^+$) are from the MSIS 2 model [43] for 2021 February 24. The isotopic enrichment of the bulk (i.e., atomic and molecular) oxygen composition is set to $\delta^{18}\text{O} = 24.15\%$ [30].

accurate $\delta^{18}\text{O}$ values for the MLT. The variation of the non-LTE corrections in the weaker $^3\text{P}_0 \leftarrow ^3\text{P}_1$ line is a direct consequence of the fact that collisionally induced transitions between these states are inhibited, and therefore more prone to environmental conditions, owing to the temperature dependence of the collision rates. The detailed output of the chemical model (evolution of $\delta^{18}\text{O}$ values for the reservoir of atomic oxygen, resolved for fine structure, and of $^{16}\text{O}^{18}\text{O}$, vs time and altitude) is shown in Fig. 7 and described in Appendix C. After applying the non-LTE corrections, one obtains for the bulk $^{16}\text{O}/^{18}\text{O}$ ratios (i.e., comprising both molecular and atomic oxygen) values of 468 ± 44 and 382 ± 38 for 2021 February 24 and November 19, respectively. The former value agrees with the isotope ratio of $^{16}\text{O}/^{18}\text{O} = 487$ due to the Dole effect in the troposphere [17], and from stratospheric O_2 [34]. All values fall below those from the solar wind samples, 529.7 ± 1.9 and 526.8 ± 2.6 ([6] and [5], respectively); our bulk values do so even more strikingly under corrections for non-LTE. In view of the large uncertainties, this result needs to be confirmed by a more sensitive measurement to become rigorous. As a matter of fact, its uncertainties also comprise the range deduced from stratospheric ozone (Fig. 4), $^{16}\text{O}/^{18}\text{O} = 449$ to 466 [67], and 429 to 438 from asymmetric $^{18}\text{OO}_2$, which shows a diurnal variation [68]. These enrichments are thought to result from the same isotopic exchange reactions (3) and (4) discussed here, except that our study refers to a reservoir that is largely void of ozone, even in comparison to the concentration of ^{18}O .

B. Ion-neutral reactions

The preceding discussion of the role of isotopic exchange reactions in populating the $^{18}\text{O}(^3\text{P})$ triplet would be incomplete

without giving consideration to ion-neutral reactions: Thanks to the acceleration of an ion in the dipole field induced in a neutral reactant, they easily overcome the activation barrier, leading to a correspondingly high reaction rate (see e.g., Ref. [75] for a review). Their impact on the isotopic oxygen composition of the thermosphere was studied to quantify the contamination of the Lunar regolith record by the magnetospheric wind escaping from Earth [8]. Among the ion-neutral reactions relevant for the upper atmosphere, we examine those offering pathways for a fractionation of oxygen isotopes (summarized in Appendix Table VI). Reactions involving the metastable $\text{O}(^1\text{D})$ singlet, mainly produced by photolysis of O_2 and O_3 [76], are discarded: its reactivity entails a short lifetime (ibid.) and at the altitude range relevant for the study at hand its concentration falls orders of magnitude below that of ^{18}O [77]. The underlying concentrations of atomic and molecular oxygen and nitrogen are provided by an extension of the MSIS 2 model to nitric oxide [78], and were retrieved for the 2021 February 24 flight. Empirical concentrations of the ionic reactants are given by the International Reference Ionosphere (2016 version [79]), except for that of N_2^+ , which we approximately retrieve from a comparison with [8] and from the free electron concentration (which at nighttime is exceeded by that of anions only below 80 km altitude [56]). The uptake of ^{16}O and ^{18}O and of O_2 by ion-neutral reactions (entailing further isotopic fractionation) is only considered when occurring at a faster rate than reactions (3) and (4), and below 200 km altitude (layers above contribute less than 1% to the column densities measured by us). This approach identifies the resonant charge exchange between N_2^+ and $\text{O}(^3\text{P})$ or the alternative route forming NO^+ (with a branching ratio of 1:21.4) as competitive, each offering three paths for isotopic reactants. They compete with reaction (4) above 161.9 and 133.4 km altitude, respectively, merely contributing 2.5% and 5.1% to the column density of $\text{O}(^3\text{P})$. The charge transfer reaction between O^+ and O_2 becomes important at altitudes above 171.9 km, contributing at most 1.9% to the column densities deduced from the $\text{O}(^3\text{P})$ lines. For the sake of completeness, we include the radiative association of O_2 and N : Although as neutral-neutral reaction slow at the temperature minimum defining the mesopause, it starts to compete with the reverse reaction (4) at 130 km altitude thanks to the rising temperature and concentration of atomic nitrogen. Again, the largest contribution to the column density of $\text{O}(^3\text{P})$ originates from altitudes below 130 km (93%). It is therefore hardly conceivable that the errors resulting from the neglect of ion-neutral and nitrogen chemistry exceed the combined standard uncertainty of our measurements, given that 84% of the pathways altering isotopic composition are of no concern here, unless higher-order effects are considered. It is also interesting to note that ion-neutral chemistry deviates the fractionation of ^{17}O from that of kinetic (i.e., mass-dependent) fractionation $\delta^{17}\text{O} = 0.52 \delta^{18}\text{O}$ [80] by at most 1‰, while larger excursions may arise from the photodissociation of O_2 by solar Lyman- α irradiation (at λ 121.6 nm), of up to $\pm 2\%$ at around 120 km altitude, where the + sign refers to O_2 and the - sign to $\text{O}(^3\text{P})$ [8]. Whether this caveat is a concern for the study at hand requires a thorough quantum-mechanical treatment and remains to be demonstrated. However, the deviations due to ion-neutral chemistry remain well below those of stratospheric ozone (40 to 60‰, [67] with further references therein). In

conclusion, it seems appropriate to conclude that for the study at hand isotopic exchange reactions are the main contributor to the non-LTE populations of the $^{18}\text{O}(^3\text{P})$ fine structure levels.

V. SUMMARY AND OUTLOOK

As regions difficult to access, the mesosphere and lower thermosphere of Earth have been characterized by empirical methods rather than by direct measurements. Actually, the isotopic composition above the mesopause is still unknown. The simultaneous monitoring of the column densities of atomic ^{16}O and of ^{18}O , demonstrated in this work, inheres a so far unexplored potential to complement existing studies and to pioneer novel ones, not only in the upper atmosphere, but also in solar system environments (e.g., [81] for planet Mars).

The rationale of the work at hand was to remotely probe the heavy oxygen concentration in the mesosphere and lower thermosphere, so as to investigate whether the efficient mixing of the isotopic oxygen fractionation between the troposphere and the stratosphere extends to higher altitudes. The main results are:

(1) With existing technology for far-infrared spectroscopy, employing quantum cascade laser oscillators and read-out by digital fast Fourier transform spectrometers, the two ^3P fine structure lines of atomic heavy oxygen ^{18}O in the upper atmosphere are detectable in absorption against the Moon, and can be separated from their ^{16}O equivalents by adjusting Voigt profiles, or by a dedicated radiative transfer model for the mesosphere and lower thermosphere. To the best of our knowledge, this is the first detection of heavy atomic oxygen in this remote zone of the present-day atmosphere of Earth.

(2) After correction for the partitioning of ^{18}O into atomic and molecular oxygen, the deduced $^{16}\text{O}/^{18}\text{O}$ bulk ratios are incompatible with those from solar wind samples. The result from the measurement conducted on 2021 February 19 agrees with the ratios pertaining to the Dole effect in the troposphere, and to O_2 at the stratopause. In view of the combined errors of our limited observations, a stringent conclusion whether this implies, up to small deviations, an isotopic homogeneity of oxygen from the troposphere to the lower thermosphere cannot be drawn yet, also in regard to the deviating result from 2021 November 19. Likewise, the fact that our $^{16}\text{O}/^{18}\text{O}$ bulk ratios comprise the values deduced from stratospheric ozone may be coincidental rather than a footprint of isotopic exchange reactions. A more sensitive follow-up experiment, discussed below, is therefore highly desirable.

(3) The stronger $^3\text{P}_1 \leftarrow ^3\text{P}_2$ line of ^{18}O is more stable against deviations from local thermodynamic equilibrium than its $^3\text{P}_0 \leftarrow ^3\text{P}_1$ equivalent, whose collisional (de-)excitation is, to first order, forbidden, making the populations of the $^3\text{P}_0$ and $^3\text{P}_1$ levels prone to fast isotopic exchange reactions. For the $^3\text{P}_1 \leftarrow ^3\text{P}_2$ line, we derive a correction of 11 to 12% for the column density obtained from line profile fitting under local thermodynamic equilibrium. This correction is shown to hold for both campaigns, separated in space and in time, and needs to be consolidated. Our chemical model shows that it converges fast, on a ~ 1 minute timescale.

(4) The local thermodynamic equilibrium of $^{16}\text{O}(^3\text{P})$ is largely unaffected by this competition between collisional excitation and isotopic exchange, due to the low frequency of encounters with isotopically heavy reaction partners.

(5) The dependence of the absorption in the $^3\text{P}_0 \leftarrow ^3\text{P}_1$ line of ^{18}O on environmental conditions makes it a good candidate for sounding the physics of the mesosphere and lower thermosphere and its response to the global change in the troposphere and stratosphere. Such an effort needs to be accompanied by a refined model for isotopic exchange, using dedicated (rather than scaled) cross sections for the excitation of ^{18}O by collisions with O_2 and N_2 , and adding photochemistry.

The corrections required to account for non-LTE effects in $^{18}\text{O}(^3\text{P})$ and to deduce isotopic bulk ratios compare each to the relative standard deviation of the combined, statistically evaluated uncertainties of the obtained $^{16}\text{O}/^{18}\text{O}$ ratios. We therefore conclude this study with an outlook. Owing to the recent discontinuation of the SOFIA program, for the foreseeable future there will be no mission capable of far-infrared spectroscopy of the upper atmosphere at high resolution ($\lambda/\Delta\lambda \geq 10^7$), leaving us without a near-term opportunity to follow-up this pilot study. Considering that the employed detector technology is already quite advanced, the only path to higher sensitivity involves a stratospheric balloon project: Since the $^3\text{P}_{1\leftarrow 2}$ line at 4.8 THz is located on the wing of a broad water absorption feature, an experiment conducted at 40 km flight altitude with similar instrumentation would instantaneously double the sensitivity of our observations, performed at 12 km altitude, 40° elevation and under $8\ \mu\text{m}$ water vapor. Because of the difficulties to schedule airborne observations of a fast-moving object like the Moon, the integration time was limited to 1.2 hours on sky. In a 48-hour integration, a dedicated experiment would further improve the radiometric sensitivity by a factor $\sqrt{48/1.2} = 6.3$. Altogether, the random error in the resulting isotope ratio would decrease to 7‰. This could be further reduced to 5‰ by adding a second receiver array operating in the orthogonal polarization. Such a system, which does not require a large telescope, would allow us to monitor the ^{18}O fraction in the upper atmosphere at high sensitivity.

On the long term, such an endeavor might induce another definition of the line separating Earth's atmosphere from space: While altitudes of 80 to 100 km (the effective and canonical von Kármán line [82]) are useful in aerospace applications, from the viewpoint of astrobiology and for a planet supporting oxygenic metabolism like Earth, the altitude to which biological signatures can be carried by efficient atmospheric mixing seems to be more pertinent.

ACKNOWLEDGMENTS

The dedication of Abe Cheng, who untimely passed away during SOFIA's deployment to Germany, was a supportive pillar for the project. We owe the SOFIA operations and engineering teams a debt of gratitude. We thank in particular Eric Sandberg and Bill Wohler for implementing the unusual observing mode for the absorption spectroscopy against the Moon background in the SOFIA telescope control and observing software.

We acknowledge supportive and constructive remarks from two anonymous referees. This work benefited from conversations with Norbert Langer, Martin Kaufmann, and Pascal Honvault.

We thank the University of Colorado Space Weather Technology, Research and Education Center (SWx TREC) for providing pynsis, a Python wrapper for the NRLMSIS models, and gratefully acknowledge the SABER instrument data services.

GREAT is a development by the MPI für Radioastronomie and the KOSMA/Universität zu Köln, in cooperation with the DLR Institut für Optische Sensorsysteme, financed by the participating institutes, by the German Aerospace Center (DLR) under Grants 50 OK 1102, 1103, and 1104, and within the Collaborative Research Centre 956, funded by the Deutsche Forschungsgemeinschaft (DFG). SOFIA is jointly operated by the Universities Space Research Association, Inc. (USRA), under NASA Contract No. NAS2-97001, and the Deutsches SOFIA Institut (DSI) under DLR Contracts No. 50 OK 0901 and No. 50 OK 1301 to the University of Stuttgart.

$$I_\nu(h_1) = I_\nu^{(0)} e^{-\tau_\nu/\mu} + \int_{h_2}^{h_1} (\kappa_\nu^{(6)}(z)S_\nu^{(6)}(z) + \kappa_\nu^{(8)}(z)S_\nu^{(8)}(z)) \exp\left[-\int_z^{h_1} (\kappa_\nu^{(6)}(\tilde{z}) + \kappa_\nu^{(8)}(\tilde{z})) \frac{d\tilde{z}}{\mu}\right] \frac{dz}{\mu} \quad (\text{A2})$$

where $I_\nu^{(0)}$ is the spectrum of the incident lunar continuum radiation,

$$\tau_\nu = \int_{h_2}^{h_1} (\kappa_\nu^{(6)}(z) + \kappa_\nu^{(8)}(z)) dz, \quad (\text{A3})$$

the optical depth and $\mu = \cos \theta$. Thanks to the smooth variation of the integrands (as function of the distance z between the layer under consideration and the observer), no discontinuities occur and the integrals can be solved by Chebyshev quadrature of sufficiently high order, determined by a cutoff threshold and an estimate of the residual [84]. Here, a fractional cutoff of 10^{-6} is used. Equivalently, the source functions and opacities in Eq. (A2) can be approximated by Chebyshev polynomials $T_k(z)$, which allows one to obtain the solution of $I_\nu(z)$ by comparing the coefficients pertaining to the same order k . The opacity for the main isotope can then be expressed through the level populations $N_U^{(j)}$ and $N_L^{(j)}$ in the upper and lower state respectively of the transition (with $j = 6$ or $j = 8$ for the main and heavy isotope respectively),

$$\kappa_\nu^{(j)} = \frac{c^2}{8\pi \nu_{0,j}^2} N_U^{(j)} A_{UL} \phi_\nu \left(\frac{g_U N_L^{(j)}}{g_L N_U^{(j)}} - 1 \right) \quad (\text{A4})$$

with the Einstein coefficients $A_{12} = 8.54 \times 10^{-5} \text{ s}^{-1}$ and $A_{01} = 1.64 \times 10^{-5} \text{ s}^{-1}$ for the $^3P_{J=1 \rightarrow 2}$ and $^3P_{J=0 \rightarrow 1}$ transition, respectively, with rest frequencies $\nu_{0,j}$ as given in Table I and statistical weights $g_J = 2J + 1$. The profile function $\phi_\nu^{(j)}$ is a Voigt profile [83],

$$\phi_\nu^{(j)} = \frac{1}{\gamma_G^{(j)}} \sqrt{\frac{\ln 2}{\pi}} K(x, y) \quad (\text{A5})$$

APPENDIX A: LINE PROFILES AND RADIATIVE TRANSFER UNDER SPECTRAL LINE OVERLAP

Since the optical depths under consideration are moderate and because the travel time of the photons forming atomic oxygen lines is short (~ 1 msec for the sight-line in Fig. 5 considered in the MSIS 2 model [43]) with respect to fluctuations in the physicochemical conditions, the radiative transfer may be formulated in its stationary form. For two species with partially overlapping line profiles, the underlying transfer equation [83] may be expressed as

$$(\Omega \cdot \nabla) I_\nu = -(\kappa_\nu^{(6)} + \kappa_\nu^{(8)}) I_\nu + \kappa_\nu^{(6)} S_\nu^{(6)} + \kappa_\nu^{(8)} S_\nu^{(8)} \quad (\text{A1})$$

where $\Omega \cdot \nabla$ is the directional derivative, I_ν the frequency-specific intensity of the emerging spectral line, $\kappa_\nu^{(6)}$ and $\kappa_\nu^{(8)}$ are the opacities of the fine structure lines of $^{16}\text{O}(^3\text{P})$ and $^{18}\text{O}(^3\text{P})$, respectively, and $S_\nu^{(6)}$ and $S_\nu^{(8)}$ are the corresponding source functions. For a plane-parallel medium extending from altitudes h_1 to h_2 observed under a zenith angle θ , the formal solution of Eq. (2) reads

where

$$\gamma_G^{(j)} = \frac{\nu_{0,j}}{c} \Delta \nu = \frac{\nu_{0,j}}{c} \left[\frac{2k_B T \ln 2}{m^{(j)}} \right]^{1/2} \quad (\text{A6})$$

is the half-width at half-maximum of the Doppler-broadened component, $m^{(j)}$ the atomic mass of the isotope under consideration, and T the kinetic gas temperature. $K(x^{(j)}, y^{(j)})$ is the Voigt function of the dimensionless variables

$$x^{(j)} = \frac{\nu - \nu_{0,j}}{\gamma_G^{(j)} \sqrt{2}}, y^{(j)} = \frac{\Gamma_L \sqrt{\ln 2}}{\gamma_G^{(j)}} \quad (\text{A7})$$

where Γ_L is the half-width at half-maximum of the Lorentz function (for numerical values of $\Delta \nu$ and Γ_L see Table I). For the numerical evaluation of $K(x^{(j)}, y^{(j)})$ a rational approximation was used [85]. While $\gamma_G^{(j)}$ is constrained by the

TABLE IV. Reaction rate coefficients for isotopic exchange between $\text{O}(^3\text{P})$ and O_2 .

Reaction coefficients	Rate at temperature T [$\text{cm}^3 \text{s}^{-1}$]
k_{1a} [27,71] ^a	$3.4 \times 10^{-12} (300 \text{ K}/T)^{1.1}$
k_{1b} [97] ^{a,b}	$w_J k_{1a} \exp(-32 \text{ K}/T)/1.94$
k_{2a} [27,71] ^a	$w_J 2.7 \times 10^{-12} (300 \text{ K}/T)^{0.9}$
k_{2b} [98] ^{a,b}	$k_{2a} \exp(33 \text{ K}/T)/2.06$

^aThe reaction rate coefficients do not resolve the 3P_J levels of the atomic product or reactant, assumed to be equal across the $J = 0, 1$, and 2 levels. Reactions (R1b) and (R2a) require corresponding weights $w_J = 1/3$ to be stoichiometrically correct.

^bEquilibrium constants k_{1a}/k_{1b} and k_{2a}/k_{2b} are derived from first principles of statistical physics [97,98].

TABLE V. Collisional rate coefficients.

Transition $J \rightarrow J'$	Interpolating function coefficients ^a for collisions with		
		$\text{N}_2 \ ^1\Sigma_g^+$	$\text{O}_2 \ ^3\Sigma_g^-$
$0 \rightarrow 1$	p_0	-13.2162	-5.7801
	p_1	+10.0774	+2.2232
	p_2	-6.7085	-0.8833
	p_3	+2.2539	+0.1849
	p_4	-0.3847	-0.0213
	p_5	+0.0033	+0.0016
	p_6	-0.0012	-0.0001
$0 \rightarrow 2$	p_0	-15.3582	-9.9820
	p_1	+22.2369	+12.8443
	p_2	-13.9457	-6.9455
	p_3	+4.4178	+1.9383
	p_4	-0.7455	-0.2913
	p_5	+0.0646	+0.0226
	p_6	-0.0023	-0.000
$1 \rightarrow 2$	p_0	-16.9134	-3.7918
	p_1	+23.5654	+5.5095
	p_2	-14.7893	-2.9747
	p_3	+4.7450	+0.8220
	p_4	-0.8137	-0.1222
	p_5	+0.0726	+0.0095
	p_6	-0.0026	-0.0003

^aThe temperature dependence of the rate coefficients for collisional de-excitation, $C_{jj'}$ (with $j' > j$), is expressed through an interpolating function, $\ln C_{jj'} [10^{-10} \text{ cm}^3 \text{ s}^{-1}] = \sum_{k=0}^6 p_k (\ln T [\text{K}])^k$, and reproduces reduced-mass scaled tabulated values [90] with $\leq 0.18\%$ accuracy at all relevant MLT temperatures. Upward rates for collisional excitation follow from statistical equilibrium and a Maxwellian velocity distribution at temperature T , i.e., $C_{j'j} = C_{jj'} g_j / g_{j'} \exp(-(E_j - E_{j'})/k_B T)$.

temperature profile of the MSIS 2 model, the dependence of Γ_L on altitude is less evident. It can be related to the pressure $p(z)$ and temperature $T(z)$ at altitude z via

$$\Gamma_L(z) = \gamma_L p(z) \left(\frac{T_0}{T(z)} \right)^\alpha \quad (\text{A8})$$

where T_0 is the reference temperature for the pressure broadening coefficient γ_L . In the classical hard-sphere approximation and for an ideal gas, $\alpha = 0.5$ via $\Gamma_L \propto n \langle \sigma v \rangle$ where n is the particle density, σ the cross section for collisional broadening, and v the relative velocity of the collision partners. However, this approach is hampered by the scarcity of experimental determinations of γ_L and α for atomic species. The pressure broadening coefficient of the two-photon absorption of atomic oxygen, $2p^4^3P_2 \rightarrow 3p^3P_j$, by collisions with O_2 was experimentally determined at 800 K to $\gamma_L = (6.0 \pm 1.2)$ MHz/hPa, employing laser induced fluorescence [86]. The same study derives $\gamma_L = (6.90 \times 0.45)$ MHz/hPa for broadening by collisions with He, at 340 K. Whether the agreement of both values can be interpreted as an insensitivity of γ_L to temperature remains to be demonstrated; whether the pressure broadening of two-photon absorption can be adopted for one-photon absorption is doubtful. For the $X^3\Sigma_g^-$ ground state of O_2 , which has, like atomic oxygen, an electronic biradical configuration, the pressure broadening of its fine-structure line at 118 GHz by collisions with N_2 was recently computed to $\gamma_L = 1.725$ MHz/hPa (at a reference temperature

of $T_0 = 296$ K, with $\alpha = 0.7245$), applying a new potential energy surface [87].

For lack of a dedicated laboratory experiment, we adopt $\gamma_L = 6.0 \times (800 \text{ K}/T)^{0.7}$ MHz/hPa. Although the pressure broadening will be largest at the base point of our sightlines, at 51 km altitude, it is clear that the Lorentzian component will not be dominated by this layer, given its low atomic oxygen concentration. On the other hand, the mesopause, around 110 km altitude, displays a too low pressure and does not significantly contribute to pressure broadening, despite its $\text{O}(^3P)$ concentration peak (Fig. 3). Thanks to the high signal-to-noise ratio, required for the detection of the ^{18}O components, we could measure Γ_L (sightline averaged) with relative errors of 10% to 20% (Table I). As a matter of fact, the altitude interval in which the adopted pressure broadening reproduces the Γ_L values from the line profile fitting, 80 to 86 km, corresponds to the place where the opacity-weighted Lorentz width reaches its maximum and therefore dominates the corresponding line profile component.

The least-square fits to the line profiles shown in Fig. 1 are obtained by minimizing the objective function

$$\chi^2 = \frac{1}{N-1} \sum_{j=1}^N (y_j - y)^2 \quad (\text{A9})$$

over the N relevant spectral channels covering the line profiles. The data points y_j and fit function y are related to optical depths

TABLE VI. Primary reactions for ion-neutral and nitrogen chemistry at temperature T , impacting the isotopic fractionation of $O(^3P)$ and O_2 (adopted from [8], further references therein). Reaction rate coefficients are in $10^{-10} \text{ cm}^3 \text{ s}^{-1}$, except for those involving a catalyst (denoted M, in $10^{-30} \text{ cm}^6 \text{ s}^{-1}$).

Reaction			Rate coefficient	Isotopic pathways
$N^+ + O_2$	\rightarrow	$O^+ + NO$	0.464	5
$N^+ + O_2$	\rightarrow	$O_2^+ + N$	3.07	3
$N^+ + O_2$	\rightarrow	$NO^+ + O$	2.6	5
$N^+ + O$	\rightarrow	$O^+ + N$	0.01	3
$N^+ + O + M$	\rightarrow	$NO^+ + M$	$10 (300K/T)$	3
$N^+ + NO$	\rightarrow	$N_2^+ + O$	0.5	3
$N_2^+ + O$	\rightarrow	$O^+ + N_2$	0.098	3
$O^+ + O_2$	\rightarrow	$O_2^+ + O$	$6.6 T[\text{K}]^{-0.55}$	9
$O^+ + N_2$	\rightarrow	$N_2^+ + O$	$0.9 T[\text{K}]^{-0.7}$	3
$O^+ + N_2$	\rightarrow	$NO^+ + N$	0.012	3
$O^+ + NO$	\rightarrow	$NO^+ + O$	0.01	5
$O^+ + e$	\rightarrow	O	$0.04 (300K/T)^{0.7}$	3
$O_2^+ + N$	\rightarrow	$NO^+ + O$	1.8	5
$O_2^+ + NO$	\rightarrow	$NO^+ + O_2$	3.5	5
$O_2^+ + e$	\rightarrow	$O + O(^1D)$	$2.1 (300K/T)^{0.55}$	5
$O_2^+ + e$	\rightarrow	O_2	$0.04 (300K/T)^{0.7}$	3
$NO^+ + e$	\rightarrow	NO	$4300 (300K/T)^{0.80}$	3
$H^+ + O$	\rightarrow	$O^+ + H$	3.75	3
$H^+ + O_2$	\rightarrow	$O_2^+ + H$	0.117	3
$O + O + M$	\rightarrow	$O_2 + M$	$0.0047 (300K/T)^{2.0}$	3
$O_2 + N$	\rightarrow	$NO + O$	$0.15 \exp(-3600K/T)$	5
$NO + N$	\rightarrow	$N_2 + O$	$0.21 \exp(-100K/T)$	3

at zenith, $\tau_{z,v}$ by the transformation

$$y = \begin{cases} \tau_{z,v} & \text{for } \tau_{z,v} < \tau_0 \\ \tau_0(1 + \ln(\tau_{z,v}/\tau_0)) & \text{otherwise} \end{cases} \quad (\text{A10})$$

with thresholds $\tau_0 = 0.008$ and 0.004 in the $^3P_{1\leftarrow 2}$ and $^3P_{0\leftarrow 1}$ lines, respectively. The so-defined scaling is continuous across the threshold (both in y and $dy/d\tau_{z,v}$) and ensures a more accurate fit of the $^{18}\text{O}(^3P)$ spectrum despite the dominance of its ^{16}O equivalent. In addition, convergence towards local minima of Eq. (A9) was avoided by simulated annealing applied to continuous minimization [84].

APPENDIX B: TIMESCALES FOR COLLISIONAL EXCITATION

As a starting point for the timescales involved in the collisional excitation of the 3P fine structure levels of atomic oxygen, we first analyze the excitation of the main isotope, ^{16}O . Up to about 180 km altitude, the by number most important collision partner is N_2 . Its complex absorption spectrum shields the lower atmosphere from EUV radiation [88] and is required for a better understanding of the photochemistry of the molecule. In its ground state ($X^1\Sigma_g^+$ in the notation of molecular spectroscopy) the N_2 molecule is a spin zero particle (unlike the ground state of O_2), which inhibits (to first order) the collisional de-excitation of the 3P_0 level to the 3P_1 level [89]. Since state-selective rate coefficients for collisions between $O(^3P)$ and N_2 are not available, we scale the coefficients [90] of another spin zero particle, $\text{He}(^1S)$, by the

inverse square root of the reduced mass of the collision system. While this approach only accounts for the correct scaling of the Maxwellian distributions underlying the averaging of collisional cross sections, it neglects the differences between the potential energy surfaces of the compared colliding systems, which necessarily leads to inaccurate results [91]. As demonstrated in Appendix C, this approach should nevertheless be good enough for an order-of-magnitude estimate. Scaling the $^{16}\text{O}(^3P) - \text{He}(^1S)$ collisional rate coefficients at 180 K (MSIS 2 model of the mesopause for 2021 February 24) to the $^{18}\text{O}(^3P) - N_2(X^1\Sigma_g^+)$ system by a factor of $(3.20/10.96)^{1/2} = 0.54$ results in lifetimes against collisional de-excitation of 40 msec for $^3P_0 \rightarrow ^3P_1$, 2.7 msec for $^3P_1 \rightarrow ^3P_2$, and 1.6 msec for $^3P_0 \rightarrow ^3P_2$. These lifetimes are short with respect to those for spontaneous de-excitation, 15.9 and 3.1 hours for the $^3P_0 \rightarrow ^3P_1$ and $^3P_1 \rightarrow ^3P_2$ transitions, respectively, which in turn are shorter than the photochemical lifetime of atomic oxygen at 100 km altitude: ~ 116 days after its formation, the concentration of atomic oxygen drops to 37% (the $1/e$ level) of its initial value [56,74]. Consequently, the concentrations of the members of the odd oxygen family [$O_x = O(^3P)$, the excited $O(^1D)$ state, and O_3] are dominated by meridional and zonal winds, and the vertical diffusive time scale. The transport by the two latter limits the lifetime of O_x to typically a day [74]. This implies that none of these processes will alter the collisionally induced occupancy of the 3P fine-structure levels of ^{16}O and ^{18}O , established almost immediately. At the altitudes to which our study is sensitive, any isotope-selective deviation from LTE must therefore originate in a faster process. The quenching of the reactive and, with respect to the

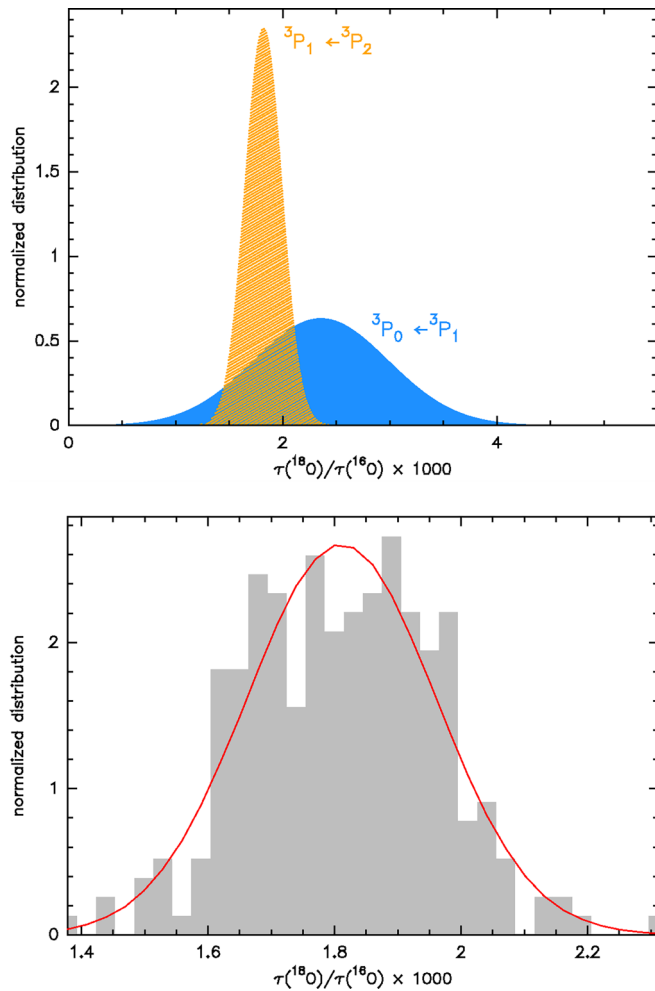


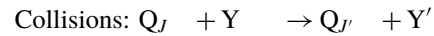
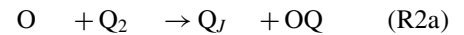
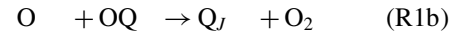
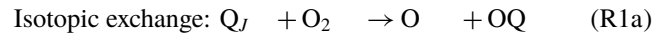
FIG. 8. Top: Comparison of the probability distributions of the optical depth ratios $\tau(^{18}\text{O})/\tau(^{16}\text{O})$ resulting from the Monte Carlo simulation of the direct fit to the 2021 February 24 data, in the $^3\text{P}_1 \leftarrow ^3\text{P}_2$ and $^3\text{P}_0 \leftarrow ^3\text{P}_1$ lines (orange and blue, respectively, and labeled to facilitate monochrome visualization). Bottom: Approximation of the distribution of the 256 variates from the Monte Carlo test by a normal (Gaussian) distribution ($^3\text{P}_1 \leftarrow ^3\text{P}_2$ line, same SOFIA flight).

^3P ground state populations of ^{16}O and ^{18}O , therefore rare ^1D state (1.97 eV above ground [92]) is not a good candidate for non-LTE in $^{18}\text{O}(^3\text{P})$, given the comparatively low energy of the ground-state levels (28 meV for $^3\text{P}_0$ [93]) and the small isotope shifts of the $^{18}\text{O}(^3\text{P})$, $\sim 0.1 \mu\text{eV}$.

APPENDIX C: MODELING OF ISOTOPE EXCHANGE REACTIONS

The level populations $N_L^{(j)}$ and $N_U^{(j)}$ are set by a network of collisional (de-)excitations and isotopic exchange reactions. As previously shown, radiative transitions between the fine structure levels are slower by several orders of magnitude and can therefore be neglected. Because spontaneous de-excitation is faster than absorption of moonlight photons by six orders of magnitude, it is included here for the sake of completeness. The system of rate equations for $^{16}\text{O}(^3\text{P})$ and $^{18}\text{O}(^3\text{P}_J)$, hereafter denoted O and Q_J , respectively, with $J = (0, 1, 2)$ then

reads



where $J \neq J'$ and $\text{Y} = \text{N}_2, \text{O}_2$ or O for the collisions and $J' > J$ for radiative decay. Isotope exchange reactions with ^{17}O , which in the VSMOW standard [4] is less abundant than ^{18}O by a factor 0.19, are omitted here. The production rates of Q_J in reactions R1b and R2a require weights w_J , because the available reaction rate coefficients are not resolved for fine structure. Here we assume the production of Q_J to occur in equal proportions, i.e., $w_J = 1/3$ for $J = (0, 1, 2)$. The reaction rate coefficients are summarized in Table IV. The rate coefficients for the excitation of Q by collisions with N_2 and O_2 are obtained from [90] and reduced mass scaling. For practical reasons, they are described by interpolating functions, provided in Table V. This approach is motivated by a recent potential energy surface for the $\text{O}(^3\text{P})\text{-N}_2(^1\Sigma_g^+)$ system [94], and largely improves the agreement between experimental and theoretical data for the collisional relaxation of vibrationally excited $v = 1 \text{ N}_2$ by $\text{O}(^3\text{P})$. Although the spin-orbit coupling is not accounted for, the potential energy surface of this system and that of $\text{O}(^3\text{P})\text{-He}(^1\text{S})$ display several similarities. They describe both the interaction between $\text{O}(^3\text{P})$ and a closed-shell particle, and therefore interact in two electronic states, $^3\Pi$ and $^3\Sigma$. The latter is located at 28.1 meV above ground, and couples to the $^3\text{P}_0$ fine-structure level of the oxygen. The equilibrium distances of the O-He complex are $5.75 a_0$ and $6.75 a_0$ for $^3\Pi$ and $^3\Sigma$, respectively [90], and in the O- N_2 complex between $5.5 a_0$ and $6.0 a_0$. We therefore scale the $\text{O}(^3\text{P})\text{-He}(^1\text{S})$ rates by the ratio $(\mu_{\text{O-He}}/\mu_{^{18}\text{O-N}_2})^{1/2} = (3.2/10.96)^{1/2} = 0.54$, where μ are the reduced masses of the systems indicated by the subscripts. For the collisions between Q and O, we make use of the rates for the $\text{O}(^3\text{P}_J) - \text{O}(^3\text{P}_{J'})$ system [55]. The temperature dependence of these rates was shown [95] to be extremely flat above 600 K, which is the temperature of the thermosphere at about 150 km altitude, while N_2 is the most important collision partner below 180 km altitude. The approximation is therefore justified. We scale the collision rates by a factor $(\mu_{\text{OO}}/\mu_{\text{OQ}})^{1/2} = 0.97$ to account for the isotopic substitution in the O-O collisional system. The initial conditions assume LTE in Q_J , adding to $\delta^{18}\text{O} = 24.15\%$ in the ^3P ground state, or $R = [\text{Q}]/[\text{O}] = 2053.63 \times 10^{-6}$. For OQ and QQ, the corresponding stochastic abundances $R_{\text{stochastic}}$ were assumed, i.e., $[\text{OQ}]/[\text{O}_2] = 2R = 4107.26 \times 10^{-6}$ and $[\text{QQ}]/[\text{O}_2] = R^2 = 4.22 \times 10^{-6}$. The above network was solved with a variable-coefficient solver for ordinary differential equations, VODE [96]. After reaching equilibrium, the relative deviation of [QQ] from the stochastic abundance amounts to up to $\Delta_{36} = (R/R_{\text{stochastic}} - 1) \simeq 20\%$. The level populations, resolved for altitude and fine structure level, are shown in Fig. 7.

APPENDIX D: AN ERROR ESTIMATOR FOR OVERLAPPING NORMAL DISTRIBUTIONS

The inequality of the $^{18}\text{O}/^{16}\text{O}$ optical depth ratios in the $^3\text{P}_1 \leftarrow ^3\text{P}_2$ and $^3\text{P}_0 \leftarrow ^3\text{P}_1$ lines entails a non-LTE population of the fine-structure levels of $^{18}\text{O}(^3\text{P})$ if the parent isotope is in LTE, while under equality both isotopes are in LTE. For the assessment of our results, we therefore need an estimator for the equality of the mean values μ_1 and μ_2 of two random variables, denoted r_1 and r_2 . We assume that both variates have a normal probability distribution, but we cannot expect that their corresponding variances σ_1 and σ_2 are equal, due to the different sensitivities of the measurements of r_1 and r_2 at 4745 GHz and 2060 GHz respectively. Estimators for the probability of equality are widely used in empirical studies. Cohen's d-estimator [99] yields the probability U_3 that the variate with the larger mean value exceeds the mean value of the other variate, and the probability A that in a random selection of a pair of variates (each from a different sample) the sample with the larger mean value also yields the larger

value in this pair (the notations of these estimators follow their use in literature, [99,100]). The description of the distributions arising in the Monte-Carlo simulations yielding the random and systematic errors (based on the spectral baseline noise and image band gain fluctuations, respectively, see Table I) by normal distributions is a good enough approximation for the wanted estimators, as long as one permits differing variances. By definition, we then obtain

$$U_3 = \int_{\mu_1}^{\infty} p_2(r)dr \text{ and } A = \int_{-\infty}^{+\infty} p_1(r) \left(\int_r^{+\infty} p_2(\tilde{r})d\tilde{r} \right) dr, \quad (\text{D1})$$

with the underlying Gaussian probability distributions

$$p_j = \frac{1}{\sigma_j \sqrt{2\pi}} \exp\left(-\frac{(r - \mu_j)^2}{2\sigma_j^2}\right), \quad j = 1, 2 \quad (\text{D2})$$

where $\mu_2 > \mu_1$. The integrations in Eqs. (D1) and (D2) are performed numerically. A demonstration of the application to the data presented in the study at hand is shown in Fig. 8.

-
- [1] S. E. Woosley and T. A. Weaver, The evolution and explosion of massive stars. II. Explosive hydrodynamics and nucleosynthesis, *Astrophys. J. Suppl. Series* **101**, 181 (1995).
- [2] D. Romano, F. Matteucci, Z. Y. Zhang, P. P. Papadopoulos, and R. J. Ivison, The evolution of CNO isotopes: A new window on cosmic star formation history and the stellar IMF in the age of ALMA, *Mon. Not. R. Astron. Soc.* **470**, 401 (2017).
- [3] T. R. Ayres, J. R. Lyons, H. G. Ludwig, E. Caffau, and S. Wedemeyer-Böhm, Is the sun lighter than the earth? Isotopic CO in the photosphere, viewed through the lens of three-dimensional spectrum synthesis, *Astrophys. J.* **765**, 46 (2013).
- [4] R. Gonfiantini, W. Stichler, and K. Rozanski, Standards and intercomparison materials distributed by the international atomic energy agency for stable isotope measurements, in *Reference and Intercomparison Materials for Stable Isotopes of Light Elements*, IAEA-TECDOC-825 (IAEA, 1995), pp. 13–29.
- [5] K. D. McKeegan, A. P. A. Kallio, V. S. Heber, G. Jarzebinski, P. H. Mao, C. D. Coath, T. Kunihiro, R. C. Wiens, J. E. Nordholt, R. W. Moses *et al.*, The oxygen isotopic composition of the sun inferred from captured solar wind, *Science* **332**, 1528 (2011).
- [6] T. R. Ireland, P. Holden, M. D. Norman, and J. Clarke, Isotopic enhancements of ^{17}O and ^{18}O from solar wind particles in the lunar regolith, *Nature (London)* **440**, 776 (2006).
- [7] K. Hashizume and M. Chaussidon, A non-terrestrial ^{16}O -rich isotopic composition for the protosolar nebula, *Nature (London)* **434**, 619 (2005).
- [8] Y. Hiraki, A. Yamada, Y. Kasai, T. Seta, and M. Ozima, Evaluation of isotopic fractionation of oxygen ions escaping from terrestrial thermosphere, *Geochim. Cosmochim. Acta* **84**, 525 (2012).
- [9] K. Terada, S. Yokota, Y. Saito, N. Kitamura, K. Asamura, and M. N. Nishino, Biogenic oxygen from Earth transported to the Moon by a wind of magnetospheric ions, *Nat. Astron.* **1**, 0026 (2017).
- [10] A. Bekker III, H. D. Holland, P. L. Wang, D. Rumble, H. J. Stein, J. L. Hannah, L. L. Coetzee, and N. J. Beukes, Dating the rise of atmospheric oxygen, *Nature (London)* **427**, 117 (2004).
- [11] H. D. Holland, Volcanic gases, black smokers, and the great oxidation event, *Geochim. Cosmochim. Acta* **66**, 3811 (2002).
- [12] J. Olejarz, Y. Iwasa, A. H. Knoll, and M. A. Nowak, The great oxygenation event as a consequence of ecological dynamics modulated by planetary change, *Nat. Commun.* **12**, 3985 (2021).
- [13] V. S. Meadows, Reflections on O_2 as a biosignature in exoplanetary atmospheres, *Astrobiology* **17**, 1022 (2017).
- [14] V. S. Meadows, C. T. Reinhard, G. N. Arney, M. N. Parenteau, E. W. Schwieterman, S. D. Domagal-Goldman, A. P. Lincowski, K. R. Stapelfeldt, H. Rauer, S. DasSarma *et al.*, Exoplanet biosignatures: Understanding oxygen as a biosignature in the context of its environment, *Astrobiology* **18**, 630 (2018).
- [15] M. Dole, The relative atomic weight of oxygen in water and in air II. A note on the relative atomic weight of oxygen in fresh water, salt water and atmospheric water vapor, *J. Chem. Phys.* **4**, 778 (1936).
- [16] G. A. Lane and M. Dole, Fractionation of oxygen isotopes during respiration, *Science* **123**, 574 (1956).
- [17] G. Hoffmann, M. Cuntz, C. Weber, P. Ciais, P. Friedlingstein, M. Heimann, J. Jouzel, J. Kaduk, E. Maier-Reimer, U. Siebt, and K. Six, A model of the Earth's Dole effect, *Glob. Biogeochem. Cycles* **18**, GB1008 (2004).
- [18] M. Bender, T. Sowers, and L. Labeyrie, The Dole Effect and its variations during the last 130,000 years as measured in the Vostok Ice Core, *Glob. Biogeochem. Cycles* **8**, 363 (1994).
- [19] S. M. Anderson, D. Hülsebusch, and K. Mauersberger, Surprising rate coefficients for four isotopic variants of $\text{O} + \text{O}_2 + \text{M}$, *J. Chem. Phys.* **107**, 5385 (1997).
- [20] Y. L. Babikov, S. N. Mikhailenko, A. Barbe, and V. G. Tyuterev, S&MPO - An information system for ozone spectroscopy on the WEB, *J. Quant. Spectrosc. Radiat. Transfer* **145**, 169 (2014).
- [21] A. Alijah, D. Lapierre, and V. Tyuterev, Non-adiabatic coupling in the ozone molecule, *Mol. Phys.* **116**, 2660 (2018).
- [22] M. H. Thiemens, The discovery of chemically produced mass independent isotope effects: The physical chemistry basis and

- applications to the early solar system, planetary atmospheres, and the origin of life, *Meteorit Planet Sci.* **54**, 231 (2019).
- [23] S. Chapman, *A Theory of Upper-atmospheric Ozone*, Memoirs of the Royal Meteorological Society (Edward Stanford, 1930)
- [24] G. Guillon, P. Honvault, R. Kochanov, and V. Tyuterev, First-principles computed rate constant for the $\text{O} + \text{O}_2$ isotopic exchange reaction now matches experiment, *J. Phys. Chem. Lett.* **9**, 1931 (2018).
- [25] P. Honvault, G. Guillon, R. Kochanov, and V. Tyuterev, Quantum mechanical study of the $^{16}\text{O} + ^{18}\text{O}^{18}\text{O} \rightarrow ^{16}\text{O}^{18}\text{O} + ^{18}\text{O}$ exchange reaction: Integral cross sections and rate constants, *J. Chem. Phys.* **149**, 214304 (2018).
- [26] S. Korutla, G. Guillon, P. Honvault, and R. R. Tammineni, Differential cross sections and product ro-vibrational distributions for $^{16}\text{O} + ^{36}\text{O}_2$ and $^{18}\text{O} + ^{32}\text{O}_2$ exchange reactions, *Chem. Phys. Lett.* **776**, 138648 (2021).
- [27] P. Fleurat-Lessard, S. Y. Grebenshchikov, R. Schinke, C. Janssen, and D. Krankowsky, Isotope dependence of the $\text{O} + \text{O}_2$ exchange reaction: Experiment and theory, *J. Chem. Phys.* **119**, 4700 (2003).
- [28] T. Rajagopala Rao, G. Guillon, S. Mahapatra, and P. Honvault, Quantum dynamics of $^{16}\text{O} + ^{36}\text{O}_2$ and $^{18}\text{O} + ^{32}\text{O}_2$ exchange reactions, *J. Chem. Phys.* **142**, 174311 (2015).
- [29] Z. Sun, D. Yu, W. Xie, J. Hou, R. Dawes, and H. Guo, Kinetic isotope effect of the $^{16}\text{O} + ^{36}\text{O}_2$ and $^{18}\text{O} + ^{32}\text{O}_2$ isotope exchange reactions: Dominant role of reactive resonances revealed by an accurate time-dependent quantum wavepacket study, *J. Chem. Phys.* **142**, 174312 (2015).
- [30] A. Pack, A. Höweling, D. C. Hezel, M. T. Stefanak, A.-K. Beck, S. T. M. Peters, S. Sengupta, D. Herwartz, and L. Folco, Tracing the oxygen isotope composition of the upper Earth's atmosphere using cosmic spherules, *Nat. Commun.* **8**, 15702 (2017).
- [31] T. Yamagami, Y. Saito, Y. Matsuzaka, M. Namiki, M. Toriumi, R. Yokota, H. Hirose, and K. Matsushima, Development of the highest altitude balloon, *Adv. Space Res.* **33**, 1653 (2004).
- [32] S. Cesare, A. Allasio, A. Anselmi, S. Dionisio, S. Mottini, M. Parisch, L. Massotti, and P. Silvestrin, The European way to gravimetry: From GOCE to NGGM, *Adv. Space Res.* **57**, 1047 (2016).
- [33] L. Y. Yeung, L. T. Murray, A. Banerjee, X. Tie, Y. Yan, E. L. Atlas, S. M. Schauffler, and K. A. Boering, Effects of ozone isotopologue formation on the clumped-isotope composition of atmospheric O_2 , *J. Geophys. Res. (Atmospheres)* **126**, e34770 (2021).
- [34] M. H. Thiemens, T. Jackson, E. C. Zipf, P. W. Erdman, and C. van Egmond, Carbon dioxide and oxygen isotope anomalies in the mesosphere and stratosphere, *Science* **270**, 969 (1995).
- [35] S. M. Smith, S. L. Vadas, W. J. Baggaley, G. Hernandez, and J. Baumgardner, Gravity wave coupling between the mesosphere and thermosphere over New Zealand, *J. Geophys. Res. Space Physics* **118**, 2694 (2013).
- [36] K. U. Grossmann, M. Kaufmann, and K. Vollmann, The fine structure emission of thermospheric atomic oxygen, *Adv. Space Res.* **19**, 595 (1997).
- [37] D. Offermann, K. U. Grossmann, P. Barthol, P. Knieling, M. Riese, and R. Trant, Cryogenic infrared spectrometers and telescopes for the atmosphere (CRISTA) experiment and middle atmosphere variability, *J. Geophys. Res. Atmos.* **104**, 16311 (1999).
- [38] K. U. Grossmann, Recent improvements in middle atmosphere remote sounding techniques: The CRISTA-SPAS experiment, *Washington DC American Geophysical Union Geophysical Monograph Series* **123**, 287 (2000).
- [39] M. G. Mlynczak, F. J. Martin-Torres, D. G. Johnson, D. P. Kratz, W. A. Traub, and K. Jucks, Observations of the $\text{O}(^3\text{P})$ fine structure line at 63 μm in the upper mesosphere and lower thermosphere, *J. Geophys. Res., [Space Phys.]* **109**, A12306 (2004).
- [40] H. Richter, C. Buchbender, R. Güsten, R. Higgins, B. Klein, J. Stutzki, H. Wiesemeyer, and H.-W. Hübers, Direct measurements of atomic oxygen in the mesosphere and lower thermosphere using terahertz heterodyne spectroscopy, *Commun. Earth Environ.* **2**, 19 (2021).
- [41] J. M. Brown, K. M. Evenson, and L. R. Zink, Laser magnetic-resonance measurement of the $^3\text{P}_1 - ^3\text{P}_2$ fine-structure splittings in ^{17}O and ^{18}O , *Phys. Rev. A* **48**, 3761 (1993).
- [42] P. De Natale, M. Bellini, W. Goetz, M. Prevedelli, and M. Inguscio, Hyperfine structure and isotope shift in the far-infrared ground-state transitions of atomic oxygen, *Phys. Rev. A* **48**, 3757 (1993).
- [43] J. T. Emmert, D. P. Drob, J. M. Picone, D. E. Siskind, M. Jones, M. G. Mlynczak, P. F. Bernath, X. Chu, E. Doornbos, B. Funke *et al.*, NRLMSIS 2.0: A whole atmosphere empirical model of temperature and neutral species densities, *Earth Space Sci.* **8**, e01321 (2021).
- [44] C. Risacher, R. Güsten, J. Stutzki, H. W. Hübers, R. Aladro, A. Bell, C. Buchbender, D. Büchel, T. Csengeri, C. Duran *et al.*, The upGREAT dual frequency heterodyne arrays for SOFIA, *J. Astronom. Instr.*, **07**, 1840014 (2018).
- [45] E. T. Young, E. E. Becklin, P. M. Marcum, T. L. Roellig, J. M. De Buizer, T. L. Herter, R. Güsten, E. W. Dunham, P. Temi, B. G. Andersson *et al.*, Early science with SOFIA, the stratospheric observatory for infrared astronomy, *Astrophys. J.* **749**, L17 (2012).
- [46] H. Richter, M. Wienold, L. Schrottke, K. Biermann, H. T. Grahn, and H.-W. Hübers, 4.7-THz local oscillator for the GREAT heterodyne spectrometer on SOFIA, *IEEE Trans. Terahertz Sci. Technol.* **5**, 539 (2015).
- [47] B. Klein, S. Hochgürtel, I. Krämer, A. Bell, K. Meyer, and R. Güsten, High-resolution wide-band fast Fourier transform spectrometers, *Astron. Astrophys.* **542**, L3 (2012).
- [48] J. P. Williams, D. A. Paige, B. T. Greenhagen, and E. Sefton-Nash, The global surface temperatures of the Moon as measured by the Diviner Lunar Radiometer Experiment, *Icarus* **283**, 300 (2017).
- [49] Y. Wu, Q. Jin, C. Li, T. Xu, W. Qi, W. Tan, X. Li, Z. Shi, H. He, S. Dai *et al.*, Unveiling the secrets of the midinfrared (3-5 μm) Moon, *Geophys. Res. Lett.* **48**, e88393 (2021).
- [50] G. Wei, X. Li, and S. Wang, Inversions of subsurface temperature and thermal diffusivity on the Moon based on high frequency of Chang'E-1 microwave radiometer data, *Icarus* **275**, 97 (2016).
- [51] S. Paine, am: Microwave through submillimeter-wave propagation tool for the terrestrial atmosphere, Astrophysics Source Code Library, record ascl:2205.002 (2022), ascl:2205.002, <https://ui.adsabs.harvard.edu/abs/2022ascl.soft05002P>

- [52] X. Guan, J. Stutzki, U. U. Graf, R. Güsten, Y. Okada, M. A. Requena-Torres, R. Simon, and H. Wiesemeyer, GREAT/SOFIA atmospheric calibration, *Astron. Astrophys.* **542**, L4 (2012).
- [53] <https://www.iram.fr/IRAMFR/GILDAS/>.
- [54] T. Csengeri, F. Wyrowski, K. M. Menten, H. Wiesemeyer, R. Güsten, J. Stutzki, S. Heyminck, and Y. Okada, SOFIA/GREAT observations of OD and OH rotational lines towards high-mass star forming regions, *Astron. Astrophys.* **658**, A193 (2022).
- [55] R. Sharma, B. Zygelman, F. von Esse, and A. Dalgarno, On the relationship between the population of the fine structure levels of the ground electronic state of atomic oxygen and the translational temperature, *Geophys. Res. Lett.* **21**, 1731 (1994).
- [56] G. Brasseur and S. Solomon, *Aeronomy of the Middle Atmosphere: Chemistry and Physics of the Stratosphere and Mesosphere*, Atmospheric and Oceanographic Sciences Library (Springer Netherlands, Dordrecht, 2006).
- [57] M. Y. Kulikov and M. V. Belikovich, Nighttime O(¹D) distributions in the mesopause region derived from SABER data, *Ann. Geophys.* **38**, 815 (2020).
- [58] N. Biver, D. Bockelée-Morvan, J. Crovisier, A. Lecacheux, U. Frisk, Å. Hjalmarson, M. Olberg, H.-G. Florén, A. Sandqvist, and S. Kwok, Submillimetre observations of comets with Odin: 2001 2005, *Planet. Space Sci.* **55**, 1058 (2007).
- [59] R. Courtin, B. M. Swinyard, R. Moreno, T. Fulton, E. Lellouch, M. Rengel, and P. Hartogh, First results of Herschel-SPIRE observations of Titan, *Astron. Astrophys.* **536**, L2 (2011).
- [60] J. Serigano, C. A. Nixon, M. A. Cordiner, P. G. J. Irwin, N. A. Teanby, S. B. Charnley, and J. E. Lindberg, Isotopic ratios of carbon and oxygen in Titan's CO using ALMA, *Astrophys. J.* **821**, L8 (2016).
- [61] C. R. Webster, P. R. Mahaffy, G. J. Flesch, P. B. Niles, J. H. Jones, L. A. Leshin, S. K. Atreya, J. C. Stern, L. E. Christensen, T. Owen *et al.*, Isotope ratios of H, C, and O in CO₂ and H₂O of the Martian atmosphere, *Science* **341**, 260 (2013).
- [62] I. R. H. G. Schroeder, K. Altwegg, H. Balsiger, J.-J. Berthelier, J. De Keyser, B. Fiethe, S. A. Fuselier, S. Gasc, T. I. Gombosi, M. Rubin *et al.*, ¹⁶O/¹⁸O ratio in water in the coma of comet 67P/Churyumov-Gerasimenko measured with the Rosetta/ROSINA double-focusing mass spectrometer, *Astron. Astrophys.* **630**, A29 (2019).
- [63] D. Kester, R. Higgins, and D. Teyssier, Derivation of sideband gain ratio for Herschel/HIFI, *Astron. Astrophys.* **599**, A115 (2017).
- [64] B. R. Bowman, W. K. Tobiska, F. A. Marcos, and C. Valladares, The j2006 empirical thermospheric density model, *J. Atmos. Sol. Terr. Phys.* **70**, 774 (2008).
- [65] G. G. Shepherd, Y.-M. Cho, V. I. Fomichev, and O. V. Martynenko, Thermospheric atomic oxygen concentrations from WINDII O+(²P → ²D) 732 nm emission: Comparisons with the NRLMSISE-00 and C-IAM models and with GUVI observations, *J. Atmos. Sol. Terr. Phys.* **147**, 50 (2016).
- [66] M. G. Mlynczak, L. A. Hunt, J. M. Russell, and B. T. Marshall, Updated SABER night atomic oxygen and implications for SABER ozone and atomic hydrogen, *Geophys. Res. Lett.* **45**, 5735 (2018).
- [67] M. H. Thiemens, History and applications of mass-independent isotope effects, *Annu. Rev. Earth Planet Sci.* **34**, 217 (2006).
- [68] T. O. Sato, K. Kuribayashi, N. Yoshida, and Y. Kasai, Diurnal variation of oxygen isotopic enrichment in asymmetric-18 ozone observed by the SMILES from space, *Geophys. Res. Lett.* **44**, 6399 (2017).
- [69] K. Mauersberger, B. Erbacher, D. Krankowsky, J. Gunther, and R. Nickel, Ozone isotope enrichment: Isotopomer-specific rate coefficients, *Science* **283**, 370 (1999).
- [70] L. Y. Yeung, J. L. Ash, and E. D. Young, Rapid photochemical equilibration of isotope bond ordering in O₂, *J. Geophys. Res. Atmos.* **119**, 10552 (2014).
- [71] P. Fleurat-Lessard, S. Y. Grebenshchikov, R. Siebert, R. Schinke, and N. Halberstadt, Theoretical investigation of the temperature dependence of the O+O₂ exchange reaction, *J. Chem. Phys.* **118**, 610 (2003).
- [72] L. Y. Yeung, M. Okumura, J. Zhang, T. K. Minton, J. T. Paci, A. Karton, J. M. L. Martin, J. P. Camden, and G. C. Schatz, O(³P) + CO₂ collisions at hyperthermal energies: Dynamics of nonreactive scattering, oxygen isotope exchange, and oxygen-atom abstraction, *J. Phys. Chem. A* **116**, 64 (2012).
- [73] R. R. Garcia, M. López-Puertas, B. Funke, D. R. Marsh, D. E. Kinnison, A. K. Smith, and F. González-Galindo, On the distribution of CO₂ and CO in the mesosphere and lower thermosphere, *J. Geophys. Res. Atmos.* **119**, 5700 (2014).
- [74] R. R. Garcia and S. Solomon, A new numerical model of the middle atmosphere. 2. Ozone and related species, *J. Geophys. Res.* **99**, 12937 (1994).
- [75] D. R. Bates, Other men's flowers Classical treatment of collisions; Massey's adiabatic criterion and ionization in flames; ion-molecule reactions; bound-free and free-free transition of electrons in ambient atomic hydrogen, *Phys. Rep.* **35**, 305 (1978).
- [76] P. J. Crutzen, Energy Conversions and Mean Vertical Motions in the High Latitude Summer Mesosphere and Lower Thermosphere, in *Mesospheric Models and Related Experiments*, Astrophysics and Space Science Library, edited by G. Fiocco (1971), Vol. 25 p. 78.
- [77] M. Nicolet, Aeronomical reactions of hydrogen and ozone, in *Mesospheric Models and Related Experiments*, Astrophysics and Space Science Library, edited by G. Fiocco (1971), Vol. 25, p. 1.
- [78] J. T. Emmert, M. Jones, D. E. Siskind, D. P. Drob, J. M. Picone, M. H. Stevens, S. M. Bailey, S. Bender, P. F. Bernath, B. Funke *et al.*, NRLMSIS 2.1: An empirical model of nitric oxide incorporated into MSIS, *JGS Space Phys.* **127**, e2022JA030896 (2022).
- [79] D. Bilitza, D. Altadill, V. Truhlik, V. Shubin, I. Galkin, B. Reinisch, and X. Huang, International reference ionosphere 2016: From ionospheric climate to real-time weather predictions, *Space Weather* **15**, 418 (2017).
- [80] E. D. Young, A. Galy, and H. Nagahara, Kinetic and equilibrium mass-dependent isotope fractionation laws in nature and their geochemical and cosmochemical significance, *Geochim. Cosmochim. Acta* **66**, 1095 (2002).
- [81] L. Rezac, P. Hartogh, R. Güsten, H. Wiesemeyer, H. W. Hübers, C. Jarchow, H. Richter, B. Klein, and N. Honingh, First detection of the 63 μm atomic oxygen line in the thermosphere of Mars with GREAT/SOFIA, *Astron. Astrophys.* **580**, L10 (2015).
- [82] J. C. McDowell, The edge of space: Revisiting the Karman Line, *Acta Astronaut.* **151**, 668 (2018), [arXiv:1807.07894](https://arxiv.org/abs/1807.07894).

- [83] C. J. Cannon, *The Transfer of Spectral Line Radiation* (Cambridge University Press, Cambridge, 1985) p. 541.
- [84] W. H. Press, S. A. Teukolsky, W. T. Vetterling, and B. P. Flannery, *Numerical Recipes in C* (Cambridge University Press, Cambridge, 1992).
- [85] J. Humlíček, Optimized computation of the Voigt and complex probability functions., *J. Quant. Spectrosc. Radiat. Transfer* **27**, 437 (1982).
- [86] D. Marinov, C. Drag, C. Blondel, O. Guaitella, J. Golda, B. Klarenaar, R. Engeln, V. Schulz-von der Gathen, and J.-P. Booth, Pressure broadening of atomic oxygen two-photon absorption laser induced fluorescence, *Plasma Sources Sci. Technol.* **25**, 06LT03 (2016).
- [87] M. Gancewski, H. Jóźwiak, E. Quintas-Sánchez, R. Dawes, F. Thibault, and P. Wcisło, Fully quantum calculations of $\text{O}_2\text{-N}_2$ scattering using a new potential energy surface: Collisional perturbations of the oxygen 118 GHz fine structure line, *J. Chem. Phys.* **155**, 124307 (2021).
- [88] M. O. Vieitez, T. I. Ivanov, W. M. G. Ubachs, B. R. Lewis, and C. A. de Lange, On the complexity of the absorption spectrum of molecular nitrogen, *J. Mol. Liq.* **141**, 110 (2008).
- [89] T. S. Monteiro and D. R. Flower, Excitation of O I and C I forbidden-line fine structure transitions by He and H_2 - A neglected selection rule, *Mon. Not. R. Astron. Soc.* **228**, 101 (1987).
- [90] F. Lique, J. Klos, M. H. Alexander, S. D. Le Picard, and P. J. Dagdigian, Fine-structure relaxation of $\text{O}(^3\text{P})$ induced by collisions with He, H and H_2 , *Mon. Not. R. Astron. Soc.* **474**, 2313 (2018).
- [91] K. M. Walker, B. H. Yang, P. C. Stancil, N. Balakrishnan, and R. C. Forrey, On the validity of collider-mass scaling for molecular rotational excitation, *Astrophys. J.* **790**, 96 (2014).
- [92] S. Civiš, P. Kubelík, M. Ferus, E. M. Zanozina, A. Pastorek, A. V. Naskidashvili, and V. E. Chernov, FTIR laboratory measurement of O I spectra in the 0.77-12.5 μm spectral range: Rydberg states and oscillator strengths, *Astrophys. J. Suppl. Series* **239**, 11 (2018).
- [93] D. Marinov, J. P. Booth, C. Drag, and C. Blondel, Measurement of the isotope shift of the $2p^4\ ^3P_2 \rightarrow 2p^3\ 3p^3\ ^3P_2$ two-photon transition of O I and a revision of the triplet energy levels of atomic oxygen, *J. Phys. B: At. Mol. Opt. Phys.* **50**, 065003 (2017).
- [94] Q. Hong, M. Bartolomei, F. Esposito, C. Coletti, Q. Sun, and F. Pirani, Reconciling experimental and theoretical vibrational deactivation in low-energy O + N_2 collisions, *Phys. Chem. Chem. Phys.* **23**, 15475 (2021).
- [95] B. Zygelman, A. Dalgarno, and R. D. Sharma, Excitation of the $^3\text{P}_{J=0,1,2}$ fine-structure levels of atomic oxygen in collisions with oxygen atoms, *Phys. Rev. A* **50**, 3920 (1994).
- [96] P. N. Brown, G. D. Byrne, and A. C. Hindmarsh, Vode: A variable-coefficient ode solver, *SIAM J. Sci. Stat. Comput.* **10**, 1038 (1989).
- [97] J. A. Kaye and D. F. Strobel, Enhancement of heavy ozone in the Earth's atmosphere?, *J. Geophys. Res.* **88**, 8447 (1983).
- [98] J. Sehested, O. J. Nielsen, H. Egsgaard, N. W. Larsen, T. S. Andersen, and T. Pedersen, Kinetic study of the formation of isotopically substituted ozone in argon, *J. Geophys. Res.* **103**, 3545 (1998).
- [99] J. Cohen, *Statistical Power Analysis for the Behavioral Sciences* (Taylor & Francis, London, 2013).
- [100] J. Ruscio, A probability-based measure of effect size: Robustness to base rates and other factors, *Psychol. Methods* **13**, 19 (2008).